Non-Destructive Evaluation for Mechanical Systems using Passive Thermal Methods

By

Christopher John Nash

Dissertation

Submitted to the Faculty of the

Graduate School of Vanderbilt University

in partial fulfillment of the requirements

for the degree of

DOCTOR OF PHILOSOPHY

in

Mechanical Engineering

August 31, 2020

Nashville, Tennessee

Approved:

Douglas Adams

Pranav Karve

Sankaran Mahadevan

Ravindra Duddu

Thomas Withrow

ACKNOWLEDGEMENTS

I would first and foremost like to thank my family for always supporting me throughout my entire academic career. I would have never had the opportunity to earn an advanced degree, let alone have completed a Ph.D, without you all. To my advisor, Dr. Doug Adams, I want to express my gratitude for the opportunity to work with you and the LASIR crew in grad school and your consistent belief in me from the moment you offered me the chance to work with you again. Your positivity, support, and constant expressions of belief in me, especially at times when I didn't have belief in myself, were huge for me. To Pranav Karve, who taught me so much, thank you for pushing me to be my best and to go the extra mile. I will always appreciate your patience and the personal investment you made into my education. To Garrett Thorne, who never failed to silently judge me for strolling in at 10 a.m. with bedhead, you've been a rock for me since I first started at LASIR as an undergrad. You've always been wise, easy-going, and easy to talk to. To Dave Koester, whose jolliness and hard work behind the scenes were all equally important to me. To Ray Bond, for teaching me so much at the outset of my graduate career. To my undergrad, Kailey Newcome, I'll always look back on our rides to and from the lab with a smile. I'm looking forward to seeing what you do next. To Dr. Tom Withrow for your support of my academic career since undergrad and for never failing to respond to a late-night email. I would also like to thank the members of my committee, Dr. Sankaran Mahadevan and Dr. Ravindra Duddu, who have both been instrumental in shaping my knowledge base, for their valuable insight. To the friends I've made in Nashville, I have always thought that I was incredibly lucky to have found such intelligent, kind, and hilarious people here. And last but not least, I would like to thank Onye Okeke for always making me laugh and for always having my back.

The material demonstrated in Chapters 2 and 3 is based on work supported by the U.S. Department of Energy's (DOE's) Office of Energy Efficiency and Renewable Energy (EERE) under the support of Task 4.2 of the Institute for Advanced Composites Manufacturing Innovation (IACMI), Award Number DE-EE006926 managed by John Winkel from DOE and John Unser from IACMI. Academic and national laboratory partners for this project are Derek Berry and David Snowberg (NREL), Aaron Stebner (Colorado School of Mines), Nathan Sharp (Purdue), Dayakar Penumadu and Stephen Young (University of Tennessee), and Douglas Adams (Vanderbilt). The industrial consortium for this project was led by Dana Swan (Arkema), Mingfu Zhang (Johns Mansville), and Stephen Nolet (TPI Composites). The views and opinions of the authors expressed in this paper or referenced documents do not

necessarily state or reflect those of the U.S. government of the identified collaborating partners. Authors acknowledge that important insight and ideas were obtained from academic and industrial collaborators during the project activities who are not being formally acknowledged in this manuscript as co-authors. Materials supplied, and manufacturing methods developed by the industrial collaborators are gratefully acknowledged.

The material presented in Chapter 4 is based upon work supported by the Department of Energy Office of Nuclear Energy under Award Number DE-NE0008712.

TABLE OF CONTENTS

LIST OF TABLES

Figure Page

LIST OF FIGURES

Figure Page

Chapter 1. Introduction and Background

Evaluation of the structural integrity of a material is crucial for ensuring safety and serviceability of mechanical systems. There are many techniques dedicated to detecting and evaluating damage in different types of materials. These evaluations can be performed during manufacturing, assembly, or the service life of mechanical systems. During manufacturing or assembly of a structural part, the structural integrity of the part must be evaluated before shipping the part out for use. *In-situ* evaluations are also performed, once a part has been installed for its use, in order to determine whether the part is close to failing due to wear and tear and needs to be replaced. Manufacturing and *in-situ* inspections can both prevent costly and dangerous failures of parts in the field [1][2][3].

A class of structural integrity evaluation methods, known as destructive testing methods, involves loading the mechanical component or system of interest until failure; and ascertaining the structural integrity based on failure characteristics. These methods typically render the component/system useless after the test, and hence are not suitable for evaluations during manufacturing or service life of the component/system. Non-destructive evaluation (NDE) techniques, on the other hand, identify flaw or potential failure locations without damaging the part in question, allowing the part to be used in the future if no issues are detected [4]. Both active and passive NDE methods can be used. Active methods involve the application of a stimulus to a material to produce a measurable response that can be related to damage. Examples of active inspection techniques include flash and lock-in thermography [5][6][7], ultrasonic inspection results [8] [9], and magnetic flux leakage [10][11].

Passive NDE does not require an input to the system being investigated, but instead leverages stimuli provided to the part in the course of normal manufacturing operations or routine system operations. Systems that naturally produce a measurable output that can be related to damage can be monitored for differences in the output that indicate flaws. Passive NDE is advantageous in that the only equipment required for NDE are sensors. No time is spent setting up actuators to provide an input to the part.

Thermal passive NDE methods can be widely applied, due to the many processes that either directly involve heat transfer or output heat as a by-product. Deviation of the thermal behavior of a material from the expected behavior

during a thermal process can indicate differences in the material's composition or geometry, which, in turn, could either form a flaw or already constitute a flaw in the material.

The two challenges discussed in this dissertation can be addressed using passive, thermal NDE methods. The first challenge, identifying flaws in fiber-reinforced polymer (FRP) composite materials, involves the detection of an unexpected thermal behavior in a region of a curing FRP composite part related to a flawed material composition. The curing process is an exothermic reaction, so the heat released during the process produces temperature responses that can be measured passively during manufacturing. These temperature measurements can be used to identify unexpected thermal behavior related to potential flaws in the composition of the composite material.

The second challenge, identifying corrosion in carbon steel nuclear power plant pipes, involves the detection of a changing thermal behavior resulting from both a change in the pipe's geometry (a thickness reduction in the pipe) and a change in the composition of the pipe (oxidation layers) at a corrosion site. The water flowing through the pipes has a different temperature than the temperature of the air surrounding the outside of the pipes, and this temperature gradient causes heat transfer to occur through the pipe. Temperature measurements can therefore be passively collected from the outside radius of the pipe while the piping system is in use in the power plant (an *in-situ* application). These temperature measurements can then be used to identify thermal behaviors associated with corrosion. The two passive, thermal NDE techniques outlined above are proposed as new techniques for their particular applications. The motivation and background information regarding the two applications of interest are discussed next.

1.1 Motivation

FRP composite materials are currently being used in a number of applications (aerospace, performance automotive, etc.) requiring high-performance, lightweight materials [12][13][14][15]. There are a number of other (high-volume) industries (wind, consumer automotive, and compressed gas storage [16]) that might benefit from the use of FRP composites as well. However, higher cost and longer manufacturing lead times associated with FRP composites hinder their utilization in high-volume industries. As a result, improvements to the manufacturing process that reduce cost, increase energy efficiency, and improve production speed are high priorities within the composites industry [17]. A real-time cure monitoring technique that enables passive detection and localization of potential curing abnormalities during the manufacturing process can help in process optimization, improvement of part quality, and

material characterization. This, in turn, can contribute to reducing the time and cost of manufacturing [18]. Adaptive decision-making regarding cycle time, energy usage, and potential flaw repair during the manufacturing process requires real-time measurement or estimation of process parameters, such as the temperature or degree of cure. Surface as well as internal temperature and degree of cure values in a curing composite part can, potentially, be used for residual stress estimation [18][19][20], as well as identification of manufacturing flaws related to resin distribution. Performing these analyses passively and in real time (during the manufacturing process), as opposed to after manufacturing is completed, can reduce post-manufacturing inspection time and cost. Degree of cure estimation also provides information about the completion time of the curing process, which can improve production speed.

Pipe rupture due to wall thinning as a result of corrosion is the leading cause of accidents in nuclear power plants [21]. There are many cases of flow accelerated corrosion (FAC)-related pipe ruptures causing fatalities, power plant damage, and costly outages and repairs [3], including the pipe rupture event at the Surry Power Station in the U.S. that resulted in four casualties and extensive damage to the plant [2]. One of the most susceptible locations for wall thinning due to FAC is either at or directly downstream of pipe elbows [3][22] due to the change in flow direction. Development of non-destructive evaluation methods for the detection of wall thinning and corrosion at pipe elbows is a crucial for identifying pipe sections that are at risk of rupture and thus preventing large-scale accidents. Some of the current corrosion or wall thinning detection techniques are either costly (e.g. magnetic or robotic techniques) or cannot be performed while the power plant is active (e.g. internal inspection techniques). All of the current techniques require manual setup of equipment for each use, and some, such as ultrasonic methods, also require the removal of insulation from the pipe. A cost-effective NDE technique that can be performed while the plant is active (improving upon the temporal resolution of techniques that cannot do this) and can perform passive measurements from the pipe without the need for equipment setup or insulation removal (aside from the initial installation) would therefore be beneficial. Such a technique could be used as an initial detection method to inform plant operators of at-risk pipes to reduce the number of pipes that must be manually checked.

In this chapter, overview and background information are presented regarding topics related to both internal flaw determination in FRP composites and corrosion detection in pipes. This discussion will a) highlight the gaps in the current NDE methods used for FRP composite cure monitoring, FRP composite flaw detection, and corrosion in nuclear power plant pipes, b) provide justification for the development of the methods presented in this work, and c) discuss the goals, rationale, and requirements for the development of the proposed NDE techniques. Three techniques

will be discussed in this work, with the first two related to the identification of resin distribution-based flaws in curing FRP composites, and the third related to the identification of corrosion in nuclear power plant pipe fittings. The first technique utilizes (non-contact) infrared (IR) thermography measurements and Bayesian state estimation to monitor key process variables during the curing process of FRP composites. The second technique utilizes the correction factors outputted by the Bayesian estimation from the first technique to locate potential flaws during the curing process. The third technique will utilize surface measurements from the surface of nuclear power plant pipes and a Gaussian Process Regression (GPR) model to identify corrosion-related thickness reductions. A brief overview of the current state of cure monitoring for composite parts is provided next.

1.2 Cure Monitoring Methods for FRP Composites

1.2.1 Cure Monitoring Methods

FRP composites manufacturing is a highly variable process. The composite part is made by reinforcing a stack of fiber preforms, such as fiberglass or carbon fiber, with a polymer resin matrix. The resin is infused throughout the fiber layers in liquid form, and through a chemical reaction, the resin then cures into a solid and bonds with the fibers. The chemical reaction is exothermic, so heat is released from the resin during cure. Many resins require an external heat input to initiate the chemical reaction as well, while others cure without any external heat input (referred to as "room temperature cure" resins). Regardless of the type of cure, heat is a by-product of the curing process, and the real-time measurement of the temperature response or degree of cure during the curing process can be crucial for adaptive decision-making regarding cycle time, energy usage, and potential flaw identification and repair. Various sensing systems for in-situ cure monitoring have been reported in the literature and used in practice [18][19]. A brief overview of some of the most common sensing techniques and their capabilities is given below. Three important features of each sensing technique are: a) position of the sensors (embedded, contact, or non-contact), b) dimensionality of the field of measurement/sensing (point, line, surface, or volume), and c) ability to measure or detect the important process states (e.g., temperature or degree of cure). In general, a non-contact sensing technique that can monitor the important process states in a curing part (volume) is desirable.

Various types of embedded sensors have previously been used for either direct or indirect measurements of process states. For example, optical fiber sensors (Fabry-Perot or Bragg grating sensors) can measure a shift in the

Bragg wavelength, which can be used for temperature measurements, strain measurements, and to determine the degree of cure of the resin [18][23][24][25]. Dielectric sensors measure electrical impedance, and can be used to estimate the dielectric constant of the resin when a voltage is applied across the curing composite part [26]. Both the impedance and the dielectric constant are indicative of the resin viscosity [27], which can be used to estimate the degree of cure. Thermocouples have been used as embedded sensors to measure temperature inside a composite part both during infusion [28] and during cure [25]. Embedded thermocouple measurements can also be used both to identify the degree of cure and to monitor the flow front [28][29]. One advantage of embedded sensors is that they can be used for non-destructive evaluation during the service life of the part. However, this approach can potentially compromise the structural integrity of the part [19].

Non-embedded sensors do not risk compromising the structural integrity of the part being monitored, but they usually require an interface (or contact) with the part being monitored. For example, thermocouples can be used to measure surface temperature, instead of the internal temperature in a curing part. Dielectric sensors can also be mounted to the surface of a Ultrasonic measurements are also used for monitoring the degree of cure and flow front in the entire volume of a curing composite part [18]. An ultrasonic pulse is sent into the material, and the arrival time for the reflected pulse is indicative of the density and elastic modulus of the medium. An increase in density and elastic modulus over time can be related to an increase in the degree of cure [19]. Both contact [30] and air-coupled [31] ultrasonic sensors are used. For both of these techniques, an interface with the material is required. The coupling interface can affect the accuracy of the measurement and, therefore, the estimation of the infusion states [19][27]. Acoustic methods have also been used for cure monitoring, but they are limited to monitoring the degree of cure. For these methods, the curing part is acoustically excited, and the natural frequency shifts that occur due to the increase in stiffness of the bulk material during cure are used to estimate the degree of cure [19]. Regardless of whether an embedded or non-embedded sensor is used, time must be spent to mount or position the sensors on the composite layup before infusion, which can slow the manufacturing process. In summary, although both embedded and interface-based sensors used for cure monitoring can successfully monitor process states, they can potentially interfere with infusion operations and increase the manufacturing time.

By contrast, Infrared (IR) Thermography offers a means of cure monitoring that does not require an interface with the part being monitored. The technique uses an IR camera to measure the IR radiation emitted by an object to estimate the temperature of the object. Each pixel in the thermal image created by an IR camera is essentially a sensor,

allowing thousands of temperature measurements to be taken at each moment in time. IR thermography is, therefore, the only cure monitoring technique that provides non-contact surface temperature measurements over a large area of a curing composite part [18][19]. The placement of the camera needs to be performed only once, so the sensor placement does not contribute to increased lead time for each part in this case. IR thermography can be used to passively monitor the composite surface temperature during cure. In addition, degree of cure can be calculated using temperature measurements [18][19][32]. Thus, IR thermography is a non-contact, non-intrusive, data-rich, and passive sensing technique that can be used to monitor temperature and degree of cure during FRP composite curing processes and can, potentially, fulfill the demands of fast, high-volume manufacturing. However, the technique does require an open mold (i.e. the camera must be able to view the lay-up) in order for this technique to be applied. Table 1.1 provides a summary of the cure monitoring techniques discussed above.

Table 1. 1: Summary of Cure Monitoring Techniques ("y": yes, "n": no)

Technique	Sensor Position	Measurement Dimension	Measured Process States	
			Temperature	Degree of Cure
IR Thermography	Non-Contact	Surface	y	y
Thermocouples	Embedded/Contact	Point	y	y
Optical Fibers	Embedded	Point or Line	y	y
Dielectric Sensors	Embedded/Contact	Volume	n	y
Ultrasonic Sensors	Contact/Coupled Interface	Volume	n	y
Acoustic Sensors	Contact	Volume	n	y

1.2.2 Temperature Estimation Techniques

IR thermography can be readily used for determining process states on the part surface (e.g. the rate of change of surface temperature may enable estimation of the cure completion time), but cure monitoring through the thickness of the part requires a method to estimate the temperatures within the part. Methods for estimation of internal temperature in a body using the body's surface temperature have been extensively studied in literature, including analytical solutions (utilizing surface temperature as a boundary condition) and inverse problems [33][34][35]. For

example, eigenfunction interpolation was shown to be effective for reconstructing the internal temperatures in a body using temperature measurements on the boundary [36][37]. These methods attempt to estimate the temperature field in a body by computing a weighted sum of a finite number of eigenfunctions of the corresponding Sturm–Liouville eigenproblem. The optimal weights are obtained by minimizing the error between the measured temperature data and the weighted sum at those locations (by solving an optimization problem). Once computed, the optimal weights can be used to estimate the temperature at any other location inside the body. This technique has been shown to yield accurate results for linear heat conduction problems. However, for the nonlinear heat conduction problems (such as the one considered for the case of a curing composite), the eigenfunction interpolation is both difficult to implement and does not yield accurate results. Bayesian filtering techniques (such as the Kalman filter (KF), extended KF, unscented KF, etc. [38][39][40]) have been used to estimate internal temperatures [40][41][42] and are able to fuse the information from an approximate model and external temperature measurements. However, their utility for passive, IR-thermography-based cure monitoring for FRP composites has not been explored.

Techniques have been studied in the context of estimating internal temperatures in curing composites as well [20][40][43][44][45][46]. Forward simulation-based techniques have been utilized [46], though techniques that do not include model-data fusion can suffer from inaccuracy in the context of curing composites due to the variability in the process. The method of using a forward simulation-based estimation aided by leveraging surface temperature data has also been studied. The technique was studied only in the context of simulation-based experiments, however [45]. Thermal property estimation techniques requiring the estimation of internal temperatures have been performed using optimization-based techniques or inverse problem solutions [43][44]. However, these techniques are not suitable real-time estimation due to the high computational expense of solving the pertinent inverse problem. A recent numerical study also focused on estimation of composite material states and properties during curing using an Ensemble KF [40], though the utilization of an Ensemble KF also prohibits real-time estimation due to the computational expense. Real-time internal temperature estimation using surface data has also been performed in the context of active temperature control of a curing composite part [20].

All of the aforementioned studies were performed for resin systems with computationally inexpensive (Arrhenius or Williams-Landel-Ferry equation-based) cure kinetics models. However, the estimation of internal temperature and degree of cure for resin systems with computationally-expensive cure kinetics models, such as free-radical polymerization reactions [47], have not been studied extensively. Therefore, in summary, the previous

investigations on surface-temperature-based FRP cure monitoring suffer from at least one of the following drawbacks: a) the methodology does not consider process monitoring data and is unable to account for part-specific anomalies such as non-uniform resin distribution, b) the methodology is not fast enough to allow real-time estimation, c) the methodology is not validated by performing experimental investigation, or d) the methodology is not suitable for real-time estimation involving complex cure kinetics (such as, free-radical polymerization reactions [47]).

A methodology that addresses these drawbacks, by utilizing an approximate heat conduction model, an approximate model for the complex cure kinetics, measured surface temperature data from passive IR thermography, and a Kalman filter is discussed in this dissertation. It is shown that the method is fast enough to allow real-time estimation of process states and can potentially enable process optimization and in-situ flaw detection during the composite manufacturing process. The development of a scalable, real-time cure monitoring technique for FRP composites that integrates passive IR thermography (a data-rich sensing method) with recursive Bayesian state estimation, and an experimental investigation of the effectiveness of the proposed method for a resin system with a complex free-radical polymerization reaction with autoacceleration [47] are the key contributions of this work. The proposed methodology can provide a balance between accuracy and computational speed, which is a key requirement for industrial implementation for these resin systems.

1.3 Flaw Identification in FRP Composites

Flaws in FRP composite parts can lead to dangerous and costly failures of the parts in application [1]. In order to prevent this, manufactured composite parts are inspected for flaws before being sent out into the field. All flaw inspection techniques for FRP composites are currently performed in post-manufacturing, which contributes to the long lead times for these parts. Developing a technique to perform flaw inspection during the manufacturing process, as opposed to after, can help reduce lead times and increase the volume of FRP composites produced for new applications.

The flaws that typically cause failures in FRP composites are cracks, delaminations, debonding, and fiber breakage. Microcracks form in the matrix material and propagate over time as loads are continuously applied to the part [REF]. Delaminations occur when the bonding between two fiber layers becomes weak, and the layers begin to separate [48]. Debonds refer to instances when fibers separate from the matrix [48]. These flaws are not independent, and often one flaw will lead to another (for example, delaminations can lead to crack propagation). Occasionally, these

flaws develop in the field as a result of a damage event, but often, the genesis of the flaws occurs during the manufacturing process [49][50]. Fiber damage and misaligned fibers can occur during layup of the fiber layers before infusion or during infusion. Cracks can originate in both resin-rich regions, due to the brittle nature of low fiber-volume fraction regions of a composite, and in resin-deficient regions, due to a lower stiffness in that region compared to the surrounding areas. Delaminations typically occur in locations where there are discontinuities in the load path [48], including locations where the ratio of fiber to resin is different from that of the rest of the composite part. Debonds can also occur in regions of low resin concentration. Residual stresses built up in the composite part due to non-uniform resin distribution can also contribute to both crack initiation, delaminations, and broken or weakened fibers, along with other effects that have a negative impact on the properties of the composite part [51][52]. The technique discussed in this dissertation will focus on the identification of flaws related to non-uniform resin distribution that occur during manufacturing. Identification of the presence of non-uniform resin distribution (noted above to be an underlying cause of flaw formation) during the manufacturing process enables adaptive decision making regarding potential corrective action and, as noted above, can aid in reducing cycle times.

Post-manufacturing inspection techniques of FRP composites are trending towards entirely non-destructive techniques in order to avoid damaging the part during inspection (in other words creating a flaw in an attempt to find flaws). The most common NDE techniques for inspection of FRP composites are summarized below. Note that eddy currents are omitted from the review, as they can only be used with conductive fibers. The composites studied in this dissertation will focus on glass FRP composites. IR thermography is most often used for post-manufacturing inspection of composites to check for manufacturing flaws or damage [53][54]. Active thermography techniques such as flash thermography [5] or lock-in thermography [6][7] are used, where a heat pulse or series of pulses is applied to the part, and IR thermography is used to measure the temperature of the part surface as the heat diffuses. Thermography has also been used for monitoring between the layup and infusion steps of FRP composite manufacturing to identify layup process errors or damaged fiber sheets [55]. These techniques involve active, external heating of the parts to identify temperature gradients on the surface that can indicate a flaw is present at that location. Identifiable flaws include fiber orientation, fiber-volume fraction, voids, and delaminations. These active thermography techniques cannot be applied during cure, as the application of the heat pulse(s) may interfere with the curing process. Additionally, the application(s) of the pulse(s) can be inconsistent and non-uniform, and these active thermography techniques are typically only effective for thin composites.

Ultrasonic transducers are a very common method for flaw detection in FRP composites. Pulse-echo, pitch-catch, and through transmission ultrasonic techniques can all be used for NDE in FRP composites. Pulse-echo and pitch-catch methods are both performed by applying an ultrasonic pulse through the material and measuring the return time of reflections of the pulse. Abnormal return times indicate flaw positions in the material. The through transmission method places the receiver on the opposite side of the part from the pulse transmitter. A pulse is sent through the part, and if the pulse does not reach the receiver, a flaw is likely present at a location in the part between the transmitter and receiver. Ultrasonic techniques have been shown to produce effective results when identifying delaminations and voids but are not as effective for identifying differences in fiber-volume fraction. Disadvantages of ultrasonic techniques for NDE of FRP composites include the presence of edge effects, where the reflection of the pulse from the edge of an internal feature can produce poor results [8], and potential overlapping, scattering, and attenuation of the reflected ultrasonic waves [9].

Acoustic methods can also be applied for NDE of FRP composites. The part is excited acoustically, producing a vibrational response that can be measured. Flaws, such as cracks and delaminations, can cause both a measurable shift in the vibrational frequency of the composite part and a shift in the displacement of the part. Acoustic methods can be performed using local sensors to register local motion, or globally using acoustic sensors that measure the global motion of the component [48][9]. Acoustic emission testing is also an option for NDE. This consists placing the composite part under load and measuring acoustic emissions that occur due to the release of elastic energy. This energy releases typically occur from a flaw location, so flaw can be identified by the acoustic emission from a particular region of the part (using multiple sensors to identify the particular region). The magnitudes of the acoustic emissions are also indicative of fiber-volume fraction [49].

Dielectric sensors can be applied for post-manufacturing inspection as well. This is employed by producing an electric field in the composite part and measuring the capacitance of the material. Variations in the dielectric signatures for different regions of the part can indicate differences in composition [56]. The technique has been shown to successfully identify delaminations in composite materials.

X-ray radiography is another NDE technique sometimes used for FRP composites. Photographs are produced by applying X-rays through the composite part and onto a medium on the opposite side of the part. The spatial distributions of the amount of X-ray photons allowed to pass through the composite part are indicative of the density

distribution in the part. Flaws can be identified quantitatively from the backscatter photograph, and the technique has very good contrast [9]. Despite the detail obtained through the photograph, X-ray equipment is expensive, X-rays are potentially harmful to both the composite itself and humans, and access to both sides of a composite part, which can be impractical [8][56][57]. X-ray radiography has been shown to effectively identify cracks and fiber orientations but are not as effective for detecting fiber-volume fraction, voids, or delaminations [49]. X-ray radiography cannot be performed during manufacturing.

Terahertz ray (T-ray) spectroscopy is a non-contact NDE method performed by applying a terahertz pulse (a laser pulse) to the composite specimen and measuring the time for the pulse to reflect back to a detector. This technique has an advantage over X-ray radiography, as the T-rays are not harmful to biological tissue. The technique has been shown to be a successful method for identifying delaminations in FRP composites, as multiple reflections occur at the delamination location, while only one occurs for non-delaminated areas [8]. It has also successfully been applied for detection of water content [58] and fiber waviness [59] in FRP composites. However, the expense of the equipment and the inability to perform this technique during manufacturing are detriments to the method.

Microscopy is another method used for post-manufacturing inspection of FRP composites. The technique involves visual inspection of the part via a microscope. A scanning electron microscope can also be utilized to determine the material composition of the part in certain areas, which allows the user to determine the fiber-volume fraction in the region. This can be indicative of voids as well. [50].

Manual inspection of the surface can also be performed to search for potential flaws. Parts with a high void content and/or too high of a fiber-volume fraction will appear dry and white (or closer to the color of the fiber being used). Parts manufactured using Vacuum-assisted resin transfer molding (VARTM) can appear like this when too much air got into the part during manufacturing, creating voids as the resin hardened around the air pockets, or if less resin than intended ended up in the part. However, the surface appearance of a part is not entirely indicative of the potential flaws underneath the surface, hence more advanced methods are favorable [49].

The NDE technique discussed in this dissertation will focus on a new technique that allows for the evaluation to be performed *during* the manufacturing process. Performing NDE during the manufacturing process, as opposed to after, can speed up the flaw detection process, which, in turn, can improve the efficiency of the manufacturing process in general. Passively monitoring a curing FPR composite with IR thermography can successfully identify surface

anomalies that occur during cure. For example, as shown in Figure 1.1, a pinhole in the vacuum bag during a Vacuum-Assisted Resin Transfer Molding (VARTM) infusion was detected using passive IR thermography.

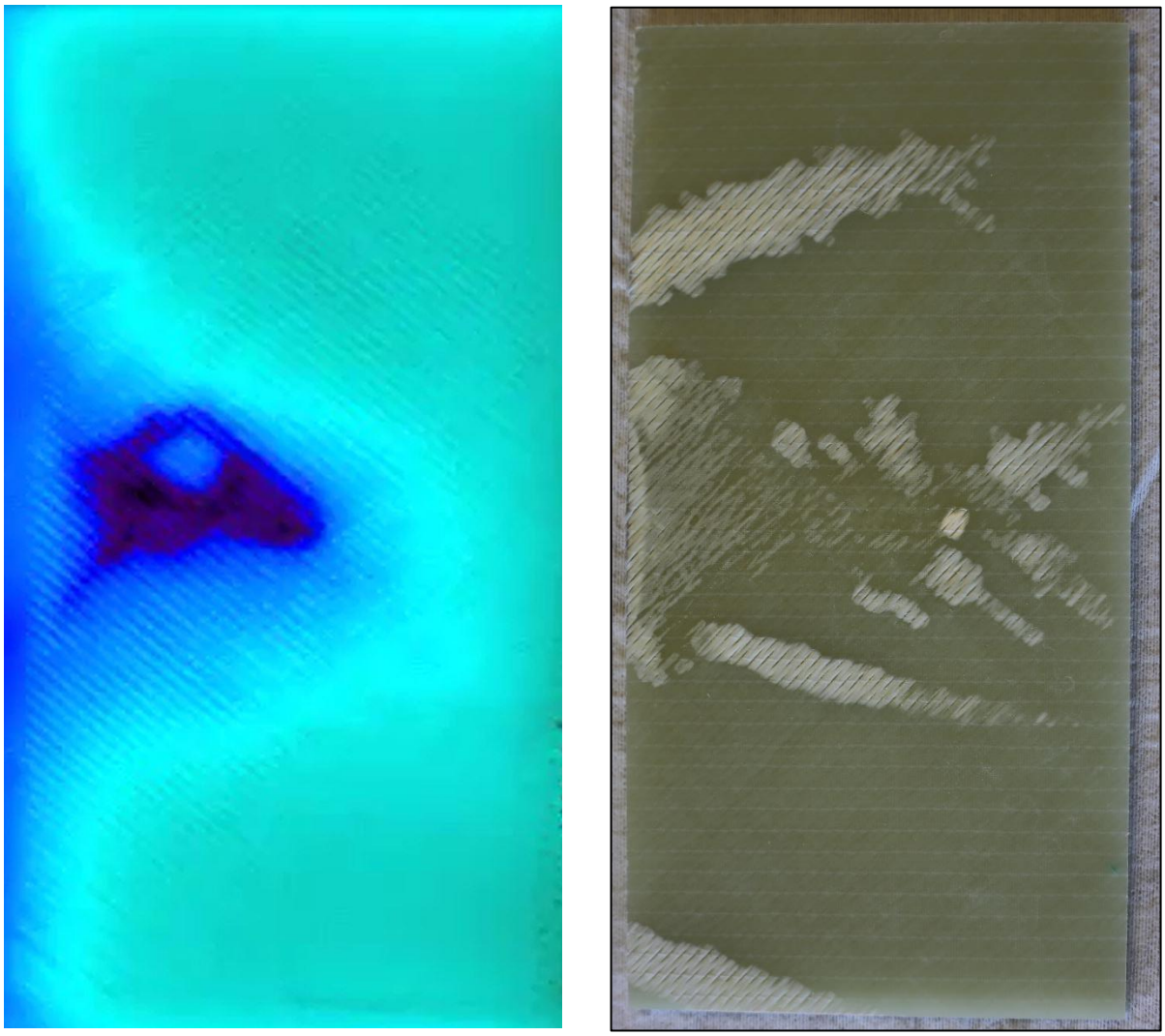

(a) (b)

Figure 1. 1: Image from a video taken using an IR camera during a VARTM infusion when there was a pinhole in the vacuum bag (a) and an image of the resulting composite panel (b)

However, in order to identify flaws below the surface, information about the sub-surface temperatures can be critical. As was discussed in Section 1.2 IR thermography can be used in conjunction with a heat transfer model

and a KF to produce internal temperature measurements in an FRP composite during the curing process. The use of a KF is crucial towards the new NDE technique. As noted in Section 1.2, KF's provide a correction term to the unfiltered model based on measurement data. This correction is indicative of a difference between the expected behavior (the model) and the actual behavior (the measurement). Assuming the model describing the curing process is accurate to a certain extent, any corrections required from the KF would indicate unexpected deviations in the process. Non-uniform resin distribution is a significant factor in temperature variations in an FRP composite, particularly for a resin system that has a room-temperature cure, due to the fact that much of the heat transfer in the part is driven by the heat generated by the resin. Therefore, regions that require a greater amount of correction from the KF can be indicative of regions with an unexpected resin distribution (fiber-volume fraction). Notably, this passive IR thermography technique is performed during the manufacturing process, whereas typical NDE techniques for FRP composites are only performed in post-manufacturing inspection. Table 1.2 shows a summary of the NDE techniques discussed above, including the new technique presented in this dissertation.

Table 1. 2: Summary of the Capabilities of FRP Composite NDE techniques to Detect Manufacturing Flaws

Technique	**Types of manufacturing flaws detected**	**Inspection during manufacturing possible?**
Active thermography	Fiber-volume fraction, voids, delaminations, fiber orientation	No
Ultrasonic sensors	Delaminations, voids	No
Acoustic sensors	Cracks, delaminations	No
Dielectric sensors	Delaminations	No
X-ray radiography	Cracks, fiber orientation	No
T-ray spectroscopy	Delaminations, water content, fiber waviness	No
Microscopy	Fiber-volume fraction, indicative of potential voids	No
Manual Inspection	Surface fiber volume fraction, indicative of potential surface voids	No
Passive thermography with KF[1]	Fiber-volume fraction, indicative of potential voids, delaminations, and cracks	Yes

1.4 Corrosion Detection in Piping Systems

Corrosion occurs in carbon steel pipes due to the buildup of oxide layers on the inner surfaces of the pipes. The oxide layers, which can include maghemite (γ-Fe_2O_3), magnetite (Fe_3O_4), and Lepidocrocite (γ-FeOOH) [22], form due to the chemical interaction of the steel with impurities in the water. These reactions break down the steel, leading to a reduction in thickness of the steel pipe beneath the oxide layers. The flow of the water inside the pipe can then erode the oxide layers that have built up, exposing the steel to the water again and repeating the cycle of wall

[1] Method proposed in this work

thickness reduction [60][61][62]. This is referred to as flow-accelerated corrosion (FAC). The removal of these oxide layers leads to the development of surface flaws, which differ depending on the flow. The inner-pipe surface features of FAC for single-phase flow (i.e. only water flow) are “scallops”, while “tiger striping” occurs for two-phase flow (i.e. water and steam). These patterns become more apparent once the degradation has occurred to a large extent [63]. In addition to scallops, pitting is also a feature of single-phase flow [22][60]. The study performed for this dissertation will focus on water temperatures (and pressures) typically applicable for single-phase flow. Regardless of the flow, these features are a result of the breakdown of the steel pipes themselves, leading to the thinning of the pipe walls. Excessive thinning of the pipe walls pipe can lead to rupture of the pipes [3][60][64]. Corrosion rates can increase depending on the flow conditions. For example, enhanced turbulence in the flow, which can occur downstream of flow restrictions that increase flow rate, can lead to an increase in corrosion rate [60]. This effect is also seen at locations where there is a change in direction of the flow, such as at T-joints or elbows. As was noted in Section 1.1, locations at or directly downstream of pipe elbows are one of the most susceptible locations for wall thinning due to FAC [3][22]. As such, the focus of the work performed for this dissertation is on the identification of wall thinning and corrosion at pipe elbows.

Many techniques have been studied for the detection of corrosion and wall thinning in power plant pipes. Ultrasonic methods (including guided wave tomography) have been shown to be effective at detecting changes in wall thickness resulting from corrosion in pipes. As described in Sections 1.2 and 1.3, ultrasonic methods are performed by applying an ultrasonic pulse to the material being evaluated and measuring the time required for the reflection of the pulse to reach a mounted transducer [21][64][65][66]. Although these methods produce accurate results for wall thickness measurement, it is less effective for detecting features, such as pitting or slotting. In addition, the insulation of the pipe must be removed (if the pipe has insulation) in order to mount the transducers to the pipe. Despite this, the technique can still produce accurate wall thickness estimates while the plant is active, though the water speed in the pipe does have an effect on measurement accuracy [67].

Magnetic NDE techniques are particularly common for wall thickness detection in ferrous materials, such as carbon steel pipes. Pulsed eddy current (PEC) testing is one of these methods. A pulsed voltage or current is applied to an electrical conductor (often a coil) placed on or around the pipe (or pipe insulation), inducing a magnetic field around the conductor. The abrupt application of the magnetic field then induces electrical eddy currents in the pipe,

and when the magnetic field is turned off, the decay of the eddy currents can be measured. This decay behavior can be related to pipe wall thickness. Notably, the technique can be used without removing the pipe insulation [68][69]. As with ultrasonics, this method can accurately detect wall thickness, but is not effective at detecting features, such as pitting or slotting. In addition, the cost and relative difficulty of use can be prohibitive [67].

Another magnetic NDE technique is magnetic flux leakage (MFL). The pipe is magnetized to the point of flux saturation using a non-contact magnet or excitation coil. Once saturated, locations with defects, such as pitting or slotting, will "leak" magnetic flux due to the local change in magnetic permeability, and the leakage field can be measured (typically using three hall sensors or other magnetic flux sensors oriented along perpendicular axes). The leakage field can then be analyzed to determine locations of defects [10][11]. MFL techniques are effective for detecting the sizing of defect features, such as slots or pitting, but cannot directly measure pipe wall thickness [67]. As with the PEC methods, MFL can also be performed with insulation on the pipe.

Internal pipe inspection methods have also been studied, including Closed-Circuit TV (CCTV) cameras. These cameras are carried through a pipe on a platform connected to a cable that controls that platform's movement. The camera records video footage of the inside of the pipe, and defects can be visually identified from the images by a plant operator. However, non-severe defects can sometimes be difficult to identify with the human eye, particularly since the images are taken inside a dark pipe. The process is also time-consuming and greatly increases inspection costs as a result [70]. Modern approaches to CCTV inspection utilize the projection of lasers onto the pipe walls to improve the quality of inspection. For example, laser scattering and light intensity-based methods have been employed to improve flaw identification and remove the human element from the technique [70][71].

Robotic inspection methods have also been studied recently for inspection both internal to [72] and external to the pipe [73][74]. Robotic inspection eliminates the need for manual inspection by plant operators, and several of the techniques described above can be performed via a robot. However, the cost of the inspection robots is likely large compared to some of the other methods discussed here.

Thermal NDE techniques that utilize thermocouples mounted to the outside of the pipe (underneath the insulation) are have not been studied in the past. Though water temperatures vary greatly across different pipe applications in power plants, in general, the difference in temperature between the water flowing in the pipe and the surrounding air temperature leads to heat transfer occurring through the pipe. The steady-state temperature on the

outside of the pipe will depend on several parameters, including the properties of the pipe and insulation, the speed of the water, the surrounding air temperature, etc. In addition, changes in the wall thickness of the pipe and the build-up of an oxide layer on the inside of the pipe can have the effect of changing the steady-state temperature of the outside of the pipe over time. This change in steady-state temperature can be measured by a thermocouple mounted on the outside of the pipe, and a relationship between the steady-state temperature and the corrosion effects (pipe wall thickness and oxide build-up) can be established by building a model. This model can then be used to estimate the amount of FAC that has occurred at a particular pipe location. This method is advantageous in that it is cost-effective, easy to implement, and can be performed passively during active plant operation without the need for manual measurements by a plant engineer. However, this technique is not likely suited for the identification of defect features, such as pitting. The development and implementation of this method are discussed in this dissertation. The strengths and weaknesses of each technique discussed above are summarized in Table 1.3.

Table 1. 3: Summary of Corrosion Detection Techniques for Carbon Steel Pipes

Technique	Is access to the inside of the pipe required?	Does insulation cause issues?	Strengths	Weaknesses
Ultrasonics	No	Yes	Can detect wall thickness accurately, can be performed while plant is active	Poor at detecting pitting and slotting, accuracy depends on flow speed, requires removal of insulation
Pulsed eddy current	No	No	Can measure wall thickness through insulation, can be performed while plant is active	Better as a screening tool, cost, user-friendliness
Magnetic flux leakage	No	No	Good at detecting sizing of defect features, can be performed through insulation, can be performed while plant is active	Cannot directly measure wall thickness
CCTV/CCD camera	Yes	No	Direct view of defects via images	Access to inside of pipe required, can only be performed during shutdown period
Robotic inspection	Sometimes	Depends on the inspection method used by the robot	Does not require manual measurement	Cost
Thermocouples[2]	No	No	Cost, ease of use, passivity, can be used while plant is active	Poor at detecting specific features

1.5 Summary of Work

The work completed for the dissertation can be summarized by three objectives:

1) Develop a temperature and degree of cure estimation technique using surface temperature measurements from IR thermography, a heat conduction model, an approximate cure kinetics model, and a Kalman Filter. The correction factors output by the Kalman Filter (equal to the product of the Kalman gain matrix and the vector of differences between the measured and model-predicted temperatures) output by this technique will

[2] Method proposed in this work

be used for Objective 2 outlined below. The contribution of this work is an accurate, full-field temperature and degree of cure estimation in a curing composite while using an approximate cure kinetics model. A journal paper detailing this work has been submitted after reviews.

2) Develop a flaw detection method for FRP composites using surface temperature measurements from IR thermography, the Kalman Filter-based state estimator from objective 1. The correction factors (which are added to the model-predicted temperatures for all points of the domain as part of the Kalman Filter) can be summed over time for each individual point in the domain to indicate which points required the greatest correction. These points correspond to the locations of the flaw(s) in the FRP composite. The contribution of this objective is a flaw detection method that can provide a high-spatial-resolution 3D map of potential flaw locations and helps to improves the efficiency of the FRP composite manufacturing process. A journal paper discussing this work is currently being prepared for submission.
3) Develop a technique for identifying FAC-induced wall thinning in pipe elbows in nuclear power plant piping systems. Measurements from thermocouples mounted to the outsides of the pipes (underneath the insulation can provide information regarding the change in steady-state temperature over the lifetime of the pipe elbow. The change from the initial steady-state temperature after installation of the elbow is indicative of the amount of corrosion that has occurred at the elbow. The contribution of this objective is a corrosion detection method that is cost-effective, can be performed while the plant is active, and requires no manual input from plant operators after installation. The likely role of this technique will be as an early-detection method to identify at-risk pipes. A journal paper discussing this work is currently being prepared for submission.

This dissertation is organized as follows: Chapter 2 discusses the Kalman Filter-based temperature and degree of cure estimation technique, Chapter 3 details the flaw detection methods, and Chapter 4 focuses on the corrosion identification technique for power plant pipes. Chapter 5 summarizes the completed work and highlights extensions of the work that can be performed in the future.

Chapter 2. Real-Time Cure Monitoring of FRP Composites using Infrared Thermography and Recursive Bayesian Filtering

In this chapter, the real-time internal temperature and degree of cure estimation technique for curing composites is described. First, the methodologies of the estimation technique itself, the simulations used for verification, and an experiment used for validation are described. The results of the verifications and validation of the method are then presented and discussed.

2.1 Methodology

In this section, an approximate model for the governing physics of heat diffusion in an FRP composite during the curing process is first described. Approximations are made regarding the dimensionality of the domain, material properties of the composite, and the exothermic heat source model. A Kalman filter, which fuses the information obtained from the (approximate) physics model (the state evolution model) and IR thermography data to enable cure monitoring, is also discussed. Simulation-based studies for the verification of the implementation and effectiveness of the technique are described as well. Lastly, a laboratory experiment used to demonstrate the cure monitoring methodology is described.

2.1.1 Computational Model of Governing Physics

2.1.1.1 Governing Equation and Spatiotemporal Discretization

The heat conduction in the composite part of interest is governed by the first law of thermodynamics. It is assumed that there is no mass transfer, and the energy loss due to radiation is negligible. The heat is generated in the part due to an exothermic chemical reaction as dictated by the cure kinetics. Therefore, the governing equation is given by:

$$\rho C_p \frac{\partial \theta(\boldsymbol{x},t)}{\partial t} - \boldsymbol{\nabla} \cdot (k \boldsymbol{\nabla} \theta(\boldsymbol{x},t)) = f(\theta(\boldsymbol{x},t), \varphi(\boldsymbol{x},t)), \text{for } \boldsymbol{x} \in \Omega, \tag{2.1}$$

where $\boldsymbol{x}$ denotes the position vector, t represents time, ρ is the density of the composite part, C_p is the specific heat capacity of the part, and k is the thermal conductivity of the part. θ is defined as temperature, which is a function of position and time, f denotes the heat per unit volume generated during the exothermic reaction, φ is the degree of cure, and $\boldsymbol{\nabla}$ is the gradient operator. FRP composite materials are heterogeneous and anisotropic. In reality, the thermal properties of resin evolve as the resin cures, creating local differences in the material properties of the composite material. There are no models available in the literature for the evolution of resin properties during cure or the final thermal properties of the cured resin. Hence, in this work, the material is assumed to be homogeneous and isotropic, and the heat conduction simulation is performed using time-invariant, effective thermal properties of the composite part. Numerical heat conduction simulations with similar assumptions have been shown to produce accurate results in the context of cure monitoring [43][44][45][46]. Heat conduction in a 2D slice (Ω) is modeled as opposed to that in a three-dimensional domain in order to reduce computation time (Figure 2.1). The curvature of the mold and some variations in the thickness of the part across its length were assumed to be negligible, and the 2D cross-section was assumed to be rectangular. Note that the simplifying assumptions (homogeneity, isotropy, reduced dimensionality, approximate geometry) allow the evaluation of the utility of the proposed methodology when using a relatively simple physics model. The investigation of the utility of simple models and easily obtainable data for cure monitoring is important to facilitate implementation of the proposed methodology in industrial setting.

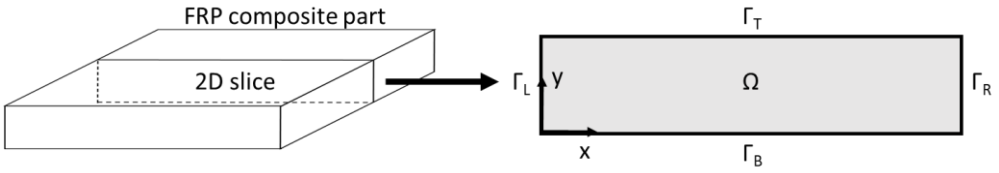

Figure 2. 1: 2D slice taken out of a 3D domain. The heat transfer physics were considered within this 2D domain

The governing equation is subjected to initial and boundary conditions. Robin [75] boundary conditions are assumed for all four boundaries, with the boundaries Γ_L, Γ_R, and Γ_T in Figure 2.1 being convective boundaries. The boundary at Γ_B was non-convective, and the heat transfer at this boundary was directly proportional to the difference between the current temperature and the mold temperature (instead of the surrounding air temperature). The initial and boundary conditions are given by:

$$(k\boldsymbol{\nabla\theta})\cdot\boldsymbol{n} = h(\boldsymbol{\theta}-\theta_{surr}\cdot\boldsymbol{e}_{ID}), \text{for } \boldsymbol{x}\in\Gamma_L\cup\Gamma_R\cup\Gamma_T, \tag{2.2a}$$

$$(k\boldsymbol{\nabla\theta})\cdot\boldsymbol{n} = h_{bot}(\boldsymbol{\theta}-\theta_{mold}\cdot\boldsymbol{e}_{ID}), \text{for } \boldsymbol{x}\in\Gamma_B, \tag{2.2b}$$

$$\boldsymbol{\theta}(\boldsymbol{x},0) = \theta_{init}\cdot\boldsymbol{e}_{ID}, \forall\,\boldsymbol{x}, \tag{2.2c}$$

where θ_{surr} is the temperature of the surrounding air, θ_{mold} is the temperature of the mold underneath the layup, and θ_{init} is the initial temperature of the part. $\boldsymbol{e}_{ID}$ is a vector of ones with the same length as $\boldsymbol{\theta}$. The resin used for the studies in this article cures at room temperature, therefore the only heat input to the system comes from the exothermic reaction. The well-known, forward in time, centered in space (FTCS) finite difference approximation of the heat equation [76] is used to discretize the governing equation. An explicit FTCS scheme was chosen as opposed to an implicit (e.g., the Crank-Nicolson) scheme in order to speed up the computation [76] and to enable cure monitoring in near-real-time. The heat equation can be approximated using FTCS as follows,

$$\boldsymbol{\theta}^i = \boldsymbol{M}\boldsymbol{\theta}^{i-1} + \boldsymbol{b} + \frac{\Delta t}{\rho C_p}\boldsymbol{f}^{i-1}, \tag{2.3}$$

where $\boldsymbol{M}$ is the diffusivity matrix, $\boldsymbol{\theta}^i$ is the temperature vector containing the temperatures of all nodes at time step *i*, $\boldsymbol{b}$ is a vector containing boundary condition terms which are not related to the temperature states, $\boldsymbol{f}^{i-1}$ is the heat generation vector at time step *i-1*, and Δt is the time step used for the time marching scheme [76]. Note that Equation 1 is a nonlinear PDE (due to the state-variable-dependent heat generation term), whereas an approximation has been made to obtain a linear discretized FTCS equation (Equation 3). The contents of the $\boldsymbol{M}$ matrix and the $\boldsymbol{b}$ vector are shown in the Appendix, where a brief derivation of the discretized form of the equations is shown.

2.1.1.2 Heat Source Modeling

The exact cure kinetics for the resin used in the experiment are unknown, but the resin's behavior during cure is known to be similar to that of (methyl methacrylate) (MMA). A cure kinetics model for the polymerization of MMA has been reported in the literature, and the free-radical polymerization reaction experiences autoacceleration during the process [47]. The model consists of a system of six coupled, nonlinear, stiff ordinary differential equations (ODEs), and coupled equations for many other state-dependent parameters. Resolving the system of ODEs for all finite difference nodes while considering the diffusion of heat is computationally expensive and difficult to perform in real time. Instead, a lookup table that estimates the cure rate ($\dot{\varphi}$) as a function of the temperature ($\boldsymbol{\theta}$) and degree of cure (φ) is created using the data generated by multiple isothermal cure kinetics simulations, and a two-dimensional linear

interpolation scheme is employed to estimate the cure rate given the current temperature and the degree of cure at each computational node at each time step. The heat generated by the resin is directly proportional to the rate of cure, and the two are related by the following equation:

The heat generated by the resin and the rate of cure, are related by the following equation:

$$\boldsymbol{f}^{i-1} = (1 - v_f) H_{resin} \rho_{resin} \dot{\boldsymbol{\varphi}}^{i-1}(\boldsymbol{\theta}^{i-1}, \boldsymbol{\varphi}^{i-1}), \tag{2.4}$$

where H_{resin} is the heat of reaction for the resin, ρ_{resin} is the density of the resin, and v_f is the fiber-volume fraction [40]. The density of the resin was assumed to be constant and was provided to the authors by the resin manufacturer, as was the heat of reaction for the resin. The rate of cure vector, $\dot{\boldsymbol{\varphi}}^{i-1}$, can be determined using the look up table described above and the temperature and degree of cure from the previous time step. The degree of cure vector for time step *i* is computed via the following approximation

$$\boldsymbol{\varphi}^{i} = \boldsymbol{\varphi}^{i-1} + \Delta t \dot{\boldsymbol{\varphi}}^{i-1}. \tag{2.5}$$

If the input vector, $\boldsymbol{u}^{i-1}$, is defined as

$$\boldsymbol{u}^{i-1} = \frac{\Delta t}{\rho C_p} \boldsymbol{f}^{i-1}, \tag{2.6}$$

then Equation 2.3 can then be expressed as:

$$\boldsymbol{\theta}^{i} = \boldsymbol{M}\boldsymbol{\theta}^{i-1} + \boldsymbol{b} + \boldsymbol{u}^{i-1}. \tag{2.7}$$

The discretized governing equation (Equation 2.7) is then used in the temperature and degree of cure estimation technique.

2.1.2 Temperature Estimation Technique

A temperature estimation technique is needed to compute the temperature (and the degree of cure) through the thickness of the part, as the IR thermography data only provides surface temperature measurements. The model described in section 2.1.1 involves approximations in the dimensionality of the problem (2D vs 3D), material behavior (time-invariance, homogeneity and isotropy), geometry, and the cure kinetics model. A temperature estimation methodology that can leverage the information contained in the measured temperature data (up to the present time) to correct estimates made by this simplified model (at the current time instant) is needed to enable accurate, real-time cure monitoring. Bayesian filtering methods, in general, and the Kalman filter and its variants, in particular, provide

a suitable alternative to carry out the fusion of information contained in the measured data and the physics model. These techniques also quantify the uncertainty in the estimate of the quantity of interest.

For nonlinear state evolution equations (similar to the one being considered here), either an extended Kalman Filter (EKF), unscented Kalman Filter (UKF), or Ensemble Kalman Filter is typically used [39][40][77]. However, the EKF technique, which relies on linearization of the state evolution equations, can suffer from instability; and the UKF technique requires Monte Carlo sampling, which reduces the speed of the temperature estimation. Ensemble Kalman filters are also prohibitive for real-time monitoring due to computational expense. The Kalman filter offers a closed form solution of the Bayesian estimation (filtering) problem based on the assumptions of linearity and normality of the state evolution and measurement models. The KF thus provides the most efficient filtering method and can be used provided the assumptions of linearity and normality are valid. The assumption of linearity is valid due to the fact that Equation 2.7 is linear for a particular time step. The normality assumption can be validated by first using a Monte Carlo simulation to generate N samples of the *entire* time history of the forward model for each node. A Chi-Square test can then be used to test whether the collection of N temperatures predicted at the final time step for a node can be described by a normal distribution for a particular significance level, α.

A brief summary of the well-known, Kalman filtering equations is given below. In these equations, the vector of mean estimated temperatures, $\boldsymbol{\mu}$, and the corresponding covariance matrix, $\boldsymbol{P}$, are calculated for each time step, *i*. $\widehat{\boldsymbol{\mu}}^i$ is the temperature vector predicted by the *unfiltered* model, and $\widehat{\boldsymbol{P}}$ is the corresponding covariance matrix. **Q** is the covariance matrix for the process error ($\boldsymbol{Q} = \sigma_p^2 \boldsymbol{I}$, where $\boldsymbol{I}$ is an identity matrix). Equation 2.7 can now be recast to yield the state evolution model as:

$$\widehat{\boldsymbol{\mu}}^i = \boldsymbol{M}\boldsymbol{\mu}^{i-1} + \boldsymbol{b} + \boldsymbol{u}^{i-1} + \boldsymbol{q}^i, \tag{2.8}$$

where $q^i \sim N(\mathbf{0}, \boldsymbol{Q})$ is the process noise. The (discretized) observation model is governed by $\boldsymbol{H}$, a matrix defining the locations (indices) of the measurement nodes. The column corresponding to the index of a measurement node has a 1 in the row corresponding to the measurement node. The rest of the matrix contains zeros. Thus, the measurement model is given by:

$$\boldsymbol{m}^i = \boldsymbol{H}\widehat{\boldsymbol{\mu}}^i + \boldsymbol{r}^i, \tag{2.9}$$

where $\boldsymbol{m}^i$ is the vector containing the measurement data at time step *i*, $\boldsymbol{r}^i \sim N(\mathbf{0}, \boldsymbol{R})$, and **R** is the covariance matrix for the measurement error ($\boldsymbol{R} = \sigma_m^2 \boldsymbol{I}$, where $\boldsymbol{I}$ is an identity matrix). If the innovation vector is defined as $\boldsymbol{v}$, and the Kalman gain matrix as $\boldsymbol{K}$, then the recursive Kalman Filter equations are as follows:

$$\widehat{\boldsymbol{P}}^i = \boldsymbol{M}\boldsymbol{P}^{i-1}\boldsymbol{M}^T + \boldsymbol{Q}, \tag{2.10}$$

$$\boldsymbol{v}^i = \boldsymbol{m}^i - \boldsymbol{H}\widehat{\boldsymbol{\mu}}^i, \tag{2.11}$$

$$\boldsymbol{S}^i = \boldsymbol{H}\widehat{\boldsymbol{P}}^i\boldsymbol{H}^T + \boldsymbol{R}, \tag{2.12}$$

$$\boldsymbol{K}^i = \widehat{\boldsymbol{P}}^i\boldsymbol{H}^T\boldsymbol{S}^{i^{-1}}, \tag{2.13}$$

$$\boldsymbol{\mu}^i = \widehat{\boldsymbol{\mu}}^i + \boldsymbol{K}^i\boldsymbol{v}^i, \tag{2.14}$$

$$\boldsymbol{P}^i = \widehat{\boldsymbol{P}}^i - \boldsymbol{K}^i\boldsymbol{S}^i\boldsymbol{K}^{i^T}. \tag{2.15}$$

In the proposed cure monitoring technique, Equations 2.8, and 2.10 through 2.15 are used in real-time to estimate internal temperatures, and Equation 2.5 is used with the mean values of temperatures at each computational node to update the degree of cure in a curing composite part.

2.1.3 Simulation-based Verification of Estimation Technique

The performance of the Kalman-filter-based cure monitoring algorithm discussed in Section 2.1.2 is evaluated using synthetic data. To this end, first, simulation data is produced using a commercial finite element program (COMSOL Multiphysics®[78]). In COMSOL, heat conduction in a rectangular domain is simulated to mimic the assumed domain for the experiment discussed in this chapter. The domain is discretized using a structured mesh of nine-node (quadratic), rectangular elements (5 mm in the x-direction in 3.75 mm in the y-direction). Two *Coefficient Form PDE* interfaces, the first describing the heat conduction and the second describing the cure kinetics, are defined in the COMSOL model. The heat transfer equation is the heat equation described in Section 2.1.1, and the heat generation is computed using Equation 2.4. The lookup table used to approximate the cure kinetics model is accessed by COMSOL, and the cure rate is interpolated using the current temperature and degree of cure values. A Multifrontal Massively Parallel Sparse (MUMPS) direct solver is used to solve the systems of differential equations at each time step. The time marching is performed using variable-order backward differentiation formulas (BDF). The heat of reaction is changed for the COMSOL model compared to the model assumed for the estimation technique, which simulates a real-life scenario where there are differences between an approximate model (the model used for the estimation technique) and the true physics (the model used for the COMSOL simulation). Robin boundary conditions are chosen for all four boundaries to mimic the assumed boundaries for the experiment discussed in this chapter. The top, left, and right boundaries are assumed to be convective boundaries, with the reference temperature being the surrounding air temperature, θ_{surr}, and the bottom boundary used a different reference temperature, θ_{mold}.

In order to generate synthetic data from the high-fidelity, COMSOL model, a (forward) heat conduction simulation is performed, and the temperature time histories on the top edge of the 2D slice (the top surface) are recorded. Gaussian white noise is added to these time histories, and this synthetic data is used as measurement data for the KF-based estimator to perform estimations. The resulting internal estimations performed by the KF-based technique are compared to the results of the COMSOL simulation to determine the accuracy of the estimation. In addition, a forward simulation of the assumed model is performed without the benefit of correction via a KF, and these results are compared to those of the COMSOL simulation and the KF-based estimator as well. This non-corrected model provides a baseline from which the improvement provided by the KF correction and measurement data is quantified.

2.1.4 Laboratory Experiments

2.1.4.1 Estimation of Effective Material Properties

Before performing the validation experiment, a calibration experiment is performed, where a genetic algorithm (GA) is employed to estimate the effective thermal properties of a fully-cured FRP composite panel manufactured in the laboratory using the same fiber and resin specifications as in the validation experiment presented later in this section. Thermocouples are embedded in the panel during manufacturing, and internal temperature data is recorded as the panel cools after being heated in an oven. A 2D heat conduction model for the cooling process is used to produce model-predicted temperatures for different combinations of properties. The thermal conductivity, k, the product of density and specific heat capacity, ρC_p, the convection coefficient, h, for convective heat transfer between the surrounding air and the composite, and the bottom surface heat transfer coefficient, h_{bot}, for heat transfer between the composite and the mold are considered as parameters to be estimated using the GA.

Though all four of these parameters are estimated in the calibration experiment, a sensitivity analysis could be used to determine parameters that significantly affect the quantity of interest (the metric used for calibration). For example, a sensitivity analysis (not reported here) revealed that only ρC_p and h_{bot} have a significant effect on the early-time cooling rate of the composite part. In the future, sensitivity analysis-informed thermal property calibration can be performed to improve the efficiency of the process and reduce the number of parameters to be calibrated. The properties that produced the best fit between the measurement data from the embedded thermocouples and the model-

predicted temperatures are returned by the GA. These properties are used as *effective, time-invariant* thermal properties of the homogeneous, isotropic 2D domain to simulate the 3D heat diffusion problem of interest. Note that determination of these effective properties may be unnecessary in an industrial setting, where material properties of manufacturing materials are typically well-known.

2.1.4.2 Validation Experiment

The temperature estimation methodology proposed in this article was validated for an FRP composite manufactured at the National Renewable Energy Lab (NREL) Composites Manufacturing Education and Technology (CoMET) facility. The manufactured part was a 2-meter-long max chord section of a wind turbine blade (the chord section closest to the root of the blade). The Vacuum-Assisted Resin Transfer Molding (VARTM) process was used for the infusion of the resin. The spar cap region of the part was chosen to test the performance of the temperature estimation method, as this region of the part did not contain any additional layup materials aside from fiberglass (other regions contained a layer of balsa wood). Although the layer of balsa wood could be included in the heat conduction model, it was avoided for simplicity. Therefore, the chosen 2D domain for the experimental validation was a vertical, 2D slice out of the spar cap region, where the x direction was the max chord length and the y direction was the max chord thickness.

The IR camera was placed above the mold at the maximum height of the stand to which it was attached in order to maximize the view of the camera. The camera view did not encompass the entire surface of the part but covered about 1775 mm of the full 2000 mm length. The camera placement and view along the width dimension is shown in Figure 2.2 (a), and the field of view along the length dimension is shown in Figure 2.2 (b). The relative location of the spar cap region as seen in the IR images recorded by the camera, the vertical plane containing embedded thermocouples, and the extents of the camera's view along the length from a top view are also shown in Figure 2.2(b). Four thermocouples were embedded in the part to provide temperature measurements for comparison to the temperature estimated by the proposed method. Note that the thermocouple measurements were *not* used as measurements for the estimation technique.

An additional thermocouple was placed at the bottom of the part between the part and the surface of the mold and was used to measure the mold temperature (θ_{mold}). This measurement was fed to the model so that the heat transfer between the part and the mold could be calculated accurately. The mean temperature values of KF-based temperature

estimates are used for comparison to the measured thermocouple data for validation. Two infusion lines were placed on top of the part and run across the full length of the part to aid in the distribution of resin. The placement of these infusion lines as well as the location of the spar cap region are shown in the IR image in Figure 2.3.

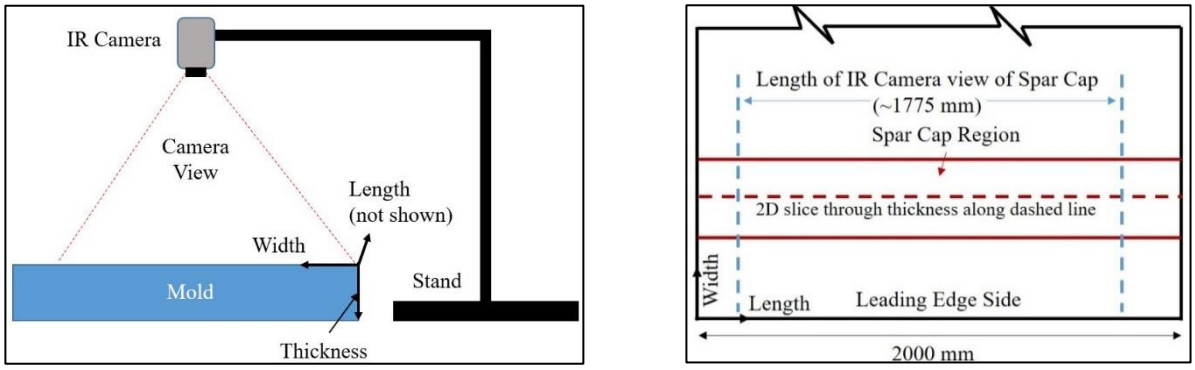

Figure 2. 2: Experimental Setup: (a) A schematic showing the position of the IR camera with respect to the VARTM mold; (b) View of the surface of the composite from the perspective of the IR camera. The extents of spar cap region, location of chosen domain for model (2D slice) and length of IR camera view are also shown. Note that image (a) shows the plane of the width and thickness dimensions, while image (b) shows the top plane of the length and width dimensions. The 2D analysis is performed in the plane of the length and thickness dimensions.

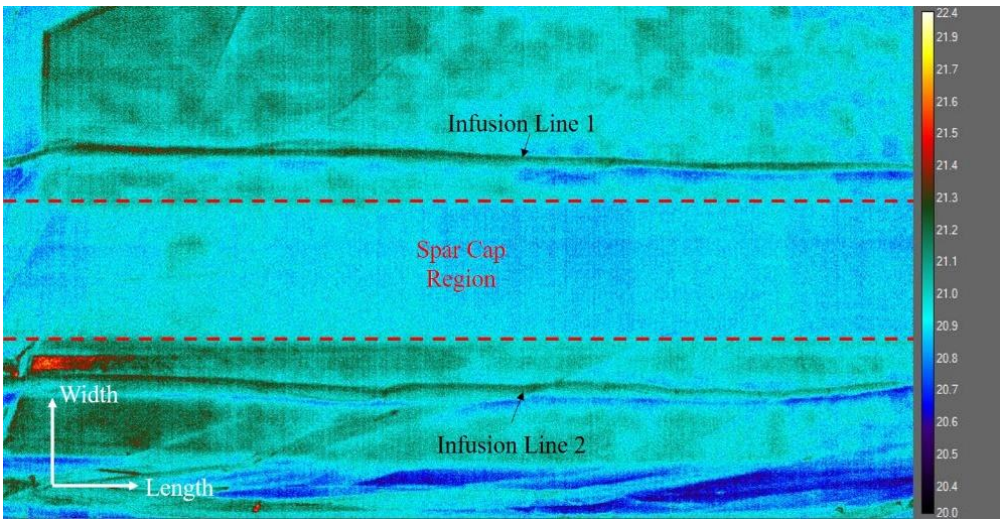

Figure 2. 3: IR image of part before infusion: the location of the infusion lines and the spar cap region are highlighted, and the temperature scale on the right is shown in Celsius

2.2 Results and Discussion

2.2.1 Estimation of Thermal Properties of Composite Material using Genetic Algorithm

A Genetic algorithm was used to estimate the thermal properties of an FRP composite part using the procedure described in Section 2.1.4.2. The finished FRP composite part used for thermal property calibration is shown in Figure 2.4. The approximate location of the cross section that was modeled to perform the calibration is also shown. Four thermocouples were embedded in the part before cure and placed along a 2D plane perpendicular to the length of the part, as shown in Figure 2.4. The approximate dimensions of this 2D slice are shown in Figure 2.5, as are the approximate locations of the thermocouples.

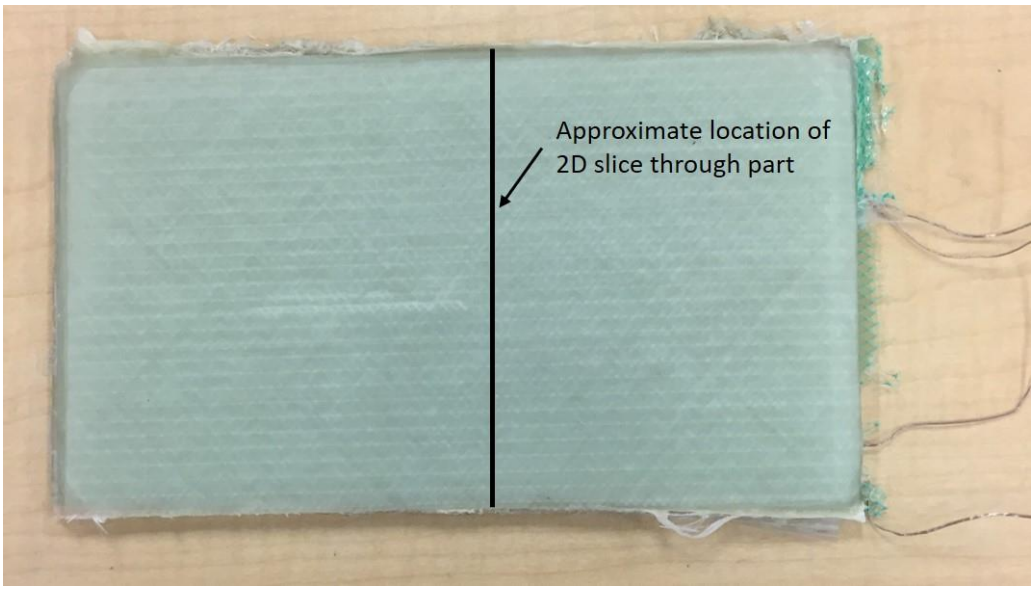

Figure 2. 4: FRP Composite panel used to estimate thermal properties with GA

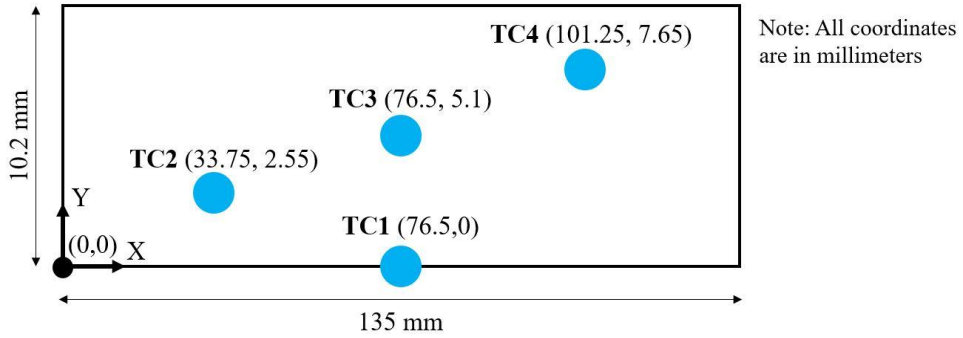

Figure 2. 5: Diagram showing the relative positions of the four thermocouples within the 2D plane through the thickness of the panel

As discussed in section 2.1.1, the part was heated in an oven, removed from the oven, and as it cooled, the temperature time histories were recorded by the thermocouples. The recorded time histories were used to estimate the material properties using a GA. The GA was run for 40 generations, with a population size of 160, a mutation probability of 0.04 and a crossover probability of 0.8. An Elitist approach was used, and parents for each generation were selected using a Roulette Wheel approach.

The results of the GA are shown in Figure 2.6 and Table 2.1. Figure 2.6 shows the result of the heat conduction simulation at the four thermocouple locations using the best-fit properties, and Table 2.1 shows the best-fit properties. The resulting error between the model-predicted temperatures when using the properties given in Table 2.1 and the measured thermocouple temperatures was less than 1% for all four thermocouple locations, indicating that the properties estimated by the algorithm can be considered to represent the material behavior well.

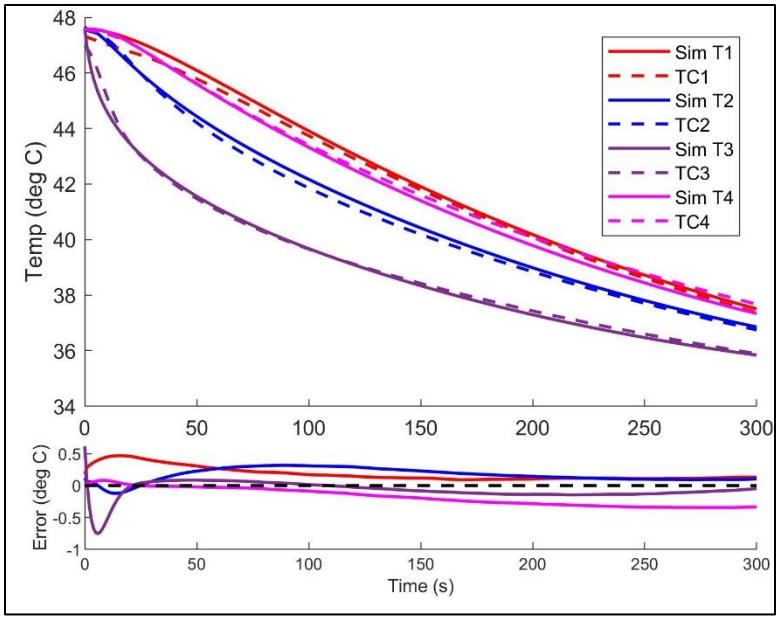

Figure 2. 6: Time histories of the temperatures; measured temperatures and temperatures predicted using properties given in Table 2.1 are shown. "Sim T1" through "Sim T4" correspond to simulated temperature variation at Points 1 through 4 in Figure 2.5, respectively, while "TC1" through "TC4" correspond to the thermocouple measurements at those points, respectively.

Table 2. 1: Properties Determined by Genetic Algorithm

Property (units)	**Value**
Thermal Conductivity, k (W/m*K)	0.42
Density*Specific Heat, ρC_p (J/(m^3*K)	1.3 x 10^6
Convection Coefficient, h (W/m^2*K)	5.6
Bottom Heat Transfer Coefficient, h_{bot} (W/m^2*K)	28.4

2.2.2 Simulation-based Verification of Estimation Technique

2.2.2.1 Determination of the Validity of Normality Assumption

The validity of the normality condition necessary for the applicability of the KF-based estimation algorithm and the performance of the temperature estimation algorithm were evaluated as described in Section 2.1.2. For both tests, the lookup table used to estimate the rate of cure was generated by assuming a 2% initiator concentration by weight. The temperature ranged from T_1 = 265 K (-8.15 ^{o}C) to T_{max} = 400 K (125.85 ^{o}C), while the degree of cure ranged from $\varphi_1 = 0.2$ to $\varphi_{max} = 1$, with 1 indicating a full cure. The range began at 0.2 because for the particular resin discussed in this work, 20% weight of reacted monomer was pre-dissolved into the bulk of the non-initiated resin. First, the normality assumption was tested using a Monte-Carlo simulation with N = 100. The FTCS forward model described in section 2.1.1 (Equation 2.7) was used to generate the samples, and a 4 x 401 nodal network was used. A time step of 1 s was used. A Chi-Square test with $\alpha = 5\%$ and $f = 5$ was run to evaluate whether a normal distribution could be used to describe the distribution of the temperatures at the final time step of the simulation. The results showed that for the three points shown in Figure 2.7, the Chi-Square metric was less than the Chi-Square bound for $\alpha = 5\%$ and $f = 5$. This indicated that the assumption of normality was valid, and, along with the validity of the linearity assumption described in Section 2.1.2, indicated that the use of a linear Kalman filter was valid.

2.2.2.2 Verification of KF-based estimator for a Pristine Part

Next, the performance of the KF-based estimation algorithm was tested using synthetically generated surface temperature data. Synthetic data was generated by adding Gaussian white noise to surface temperature data computed using a commercial finite element program (COMSOL Multphysics®). That data was fed into the estimation algorithm, and the resulting estimated mean temperatures were compared to the finite element results at the locations defined in Figure 2.7. The heat of reaction for the estimation algorithm was assumed to be 20% higher than that of the COMSOL model. In this manner, the COMSOL model was assumed to simulate the "correct", real-life behavior of the physics at play, while the state evolution model was erroneous (the heat generation was assumed to be 20% greater than the "actual" value). A 2D rectangular domain of length 2 m and thickness 7.5 mm was modeled in COMSOL and for the FTCS model. A 4 x 401 nodal network was used for the estimation algorithm, and the same (2% weight) lookup

table was used as was used above. A structured, quadrilateral mesh with 800 elements was used for the COMSOL simulation, and the same lookup table was used to define the heat source in the COMSOL model as well. A time step of 1 s was used the estimation algorithm, and a time step of 0.1 s was used for the COMSOL simulation. For the BDF solver, a maximum order of 5 and automatic time stepping were selected. The relative tolerance was set to 10^{-4}. A necessary condition for the stability of the FTCS approximation is that the Courant-Friedrichs-Lewy (CFL) condition must be met. The CFL condition, which is defined as:

$$CFL_x = \frac{k\Delta t}{\rho C_p \Delta x^2} < 0.5, \tag{3.1a}$$

$$CFL_y = \frac{k\Delta t}{\rho C_p \Delta y^2} < 0.5, \tag{3.1b}$$

was met for the chosen properties and network, with CFL_x and CFL_y equaling 0.013 and 0.052, respectively. For both the algorithm and the COMSOL simulation, k, ρC_p, h, and h_{bot} were set equal to the values determined by the GA (given in Table 2.1). θ_{surr} and the initial temperatures for each node in the network were all set equal to 20.87 °C (the average initial temperature measured by the IR camera for the experiment outlined in Section 2.1.4). θ_{mold} was set equal to the time history temperature data collected by the mold thermocouple referenced in Section 2.1.4.

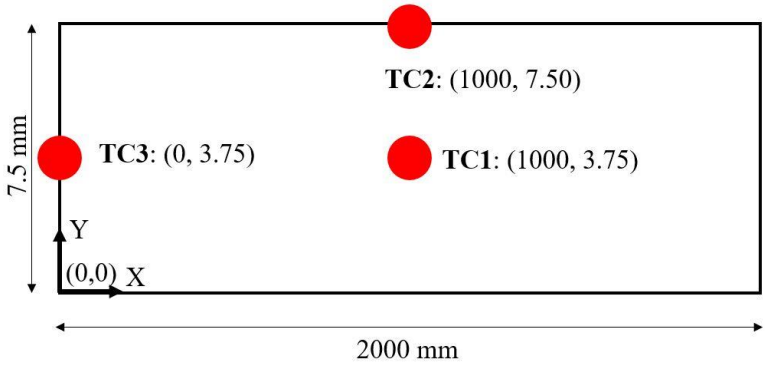

Figure 2. 7: Diagram indicating the relative locations of the points of interest (presented as "thermocouples") within the domain for simulation-based verification

The data from 400 top surface points corresponding to 400 top surface nodes in the FD network were extracted from COMSOL, with the center point (Point 2 in Figure 2.7) being the one surface node that was excluded

as a measurement point. The temperature recorded at these 400 points simulated the use of IR thermography for the surface measurements, which allows for many points to be used as measurement points. Gaussian white noise was added to the COMSOL surface temperature data as measurement noise (standard deviation, 0.1°C). The process noise and the measurement noise for the Kalman filter were also assumed to have a standard deviation of 0.1°C. The mean estimated temperatures of the algorithm at the three points of interest are shown in Figure 2.8 (a) through 2.8 (c), the error between the estimation and the COMSOL simulation at those points is shown in Figure 2.8 (d), and the degree of cure estimates and COMSOL predictions are shown in Figure 2.9. The FTCS simulation results are also included in Figures 2.8 and 2.9 for comparison. The temperature estimation algorithm is denoted by "KF" in both figures.

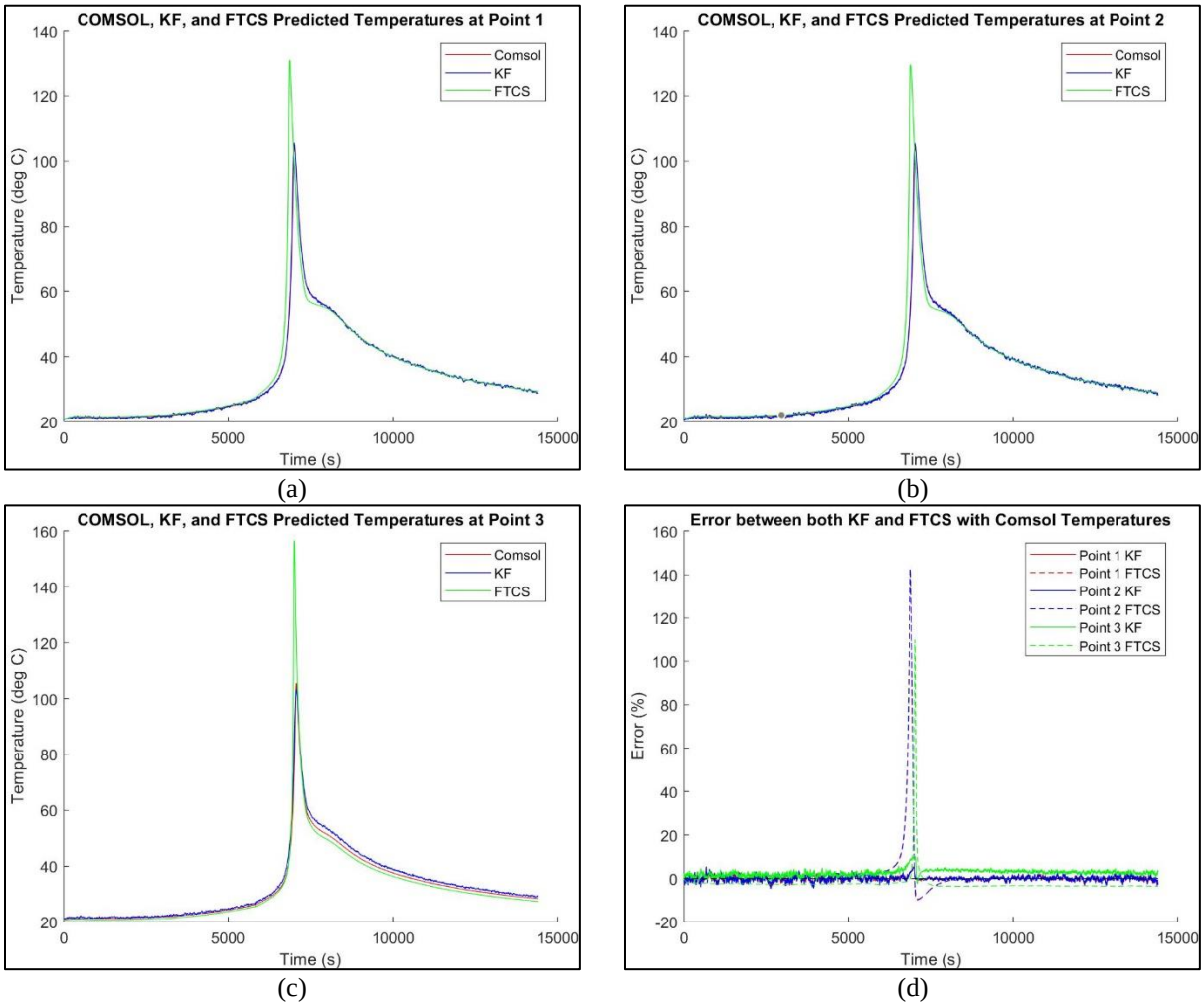

Figure 2. 8: Temperature and Error Plots Showing Algorithm Results Compared to COMSOL

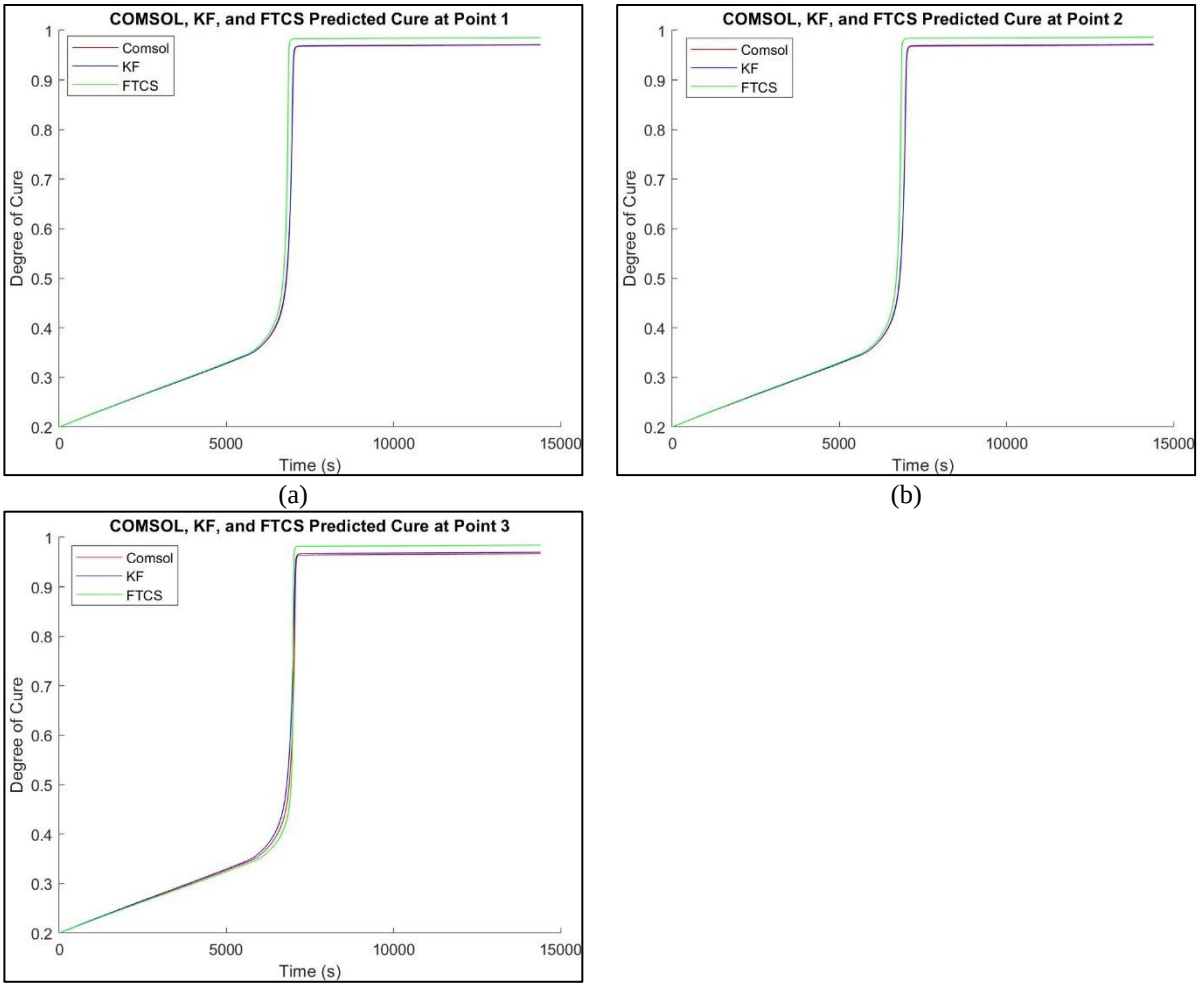

Figure 2. 9: Estimated Degree of Cure over Time for the COMSOL simulation, Estimation Algorithm, and FTCS Forward Simulation

The results shown in Figures 2.8 and 2.9 indicate that the use of the surface temperature measurements in conjunction with a Kalman Filter was able to improve the accuracy of the erroneous model assumed for the FTCS forward simulation (that is, the erroneous state evolution equation). The maximum error between the temperature predictions of the FD simulation and the COMSOL simulation at all three points of interest exceeded 100% when using the stand-alone FTCS model, but this was reduced to less than 6% at Points 1 and 2 and less than 10% at Point 3 when using the Kalman Filter. Figure 2.9 shows that the accuracy of the degree of cure estimates were also improved with use of the KF, with the COMSOL degree of cure predictions nearly overlapping with the degree of cure estimated by the algorithm.

2.2.3 Laboratory Experiment and Estimation Results

The experimental setup was described in Section 2.1.4. The model outlined in Section 2.1.2 was used in conjunction with experimental surface temperature to estimate internal temperatures of a curing composite part. Surface temperature data was collected on the curing composite part using an IR camera at 1 Hz for 11,220 seconds, starting just before infusion began and ending during the cooling period after the exothermic reaction of the resin had completed. Both a low-pass filter and a median filter (to remove measurement dropouts that result from the IR camera performing automatic recalibrations to maintain accuracy) were applied to the IR surface temperature data before using it in the temperature estimation method.

A 2D slice of thickness (width) 7.5 mm and length 2 m was modeled to obtain the state evolution model (using the FTCS scheme discussed in section 2.1.1). The thickness for the assumed rectangular domain was approximated as 7.5 mm based on thickness measurements of the max chord part after the part was de-molded, while a length of 2 m was chosen to match the length of the max chord section. The properties estimated using the GA discussed in Section 2.2.1, given in Table 2.1, were used in the heat conduction model. The fiber-volume fraction was assumed to be v_f = 0.6, as this was the target value for the spar cap region. A 2% initiator concentration by weight was used for the resin in the experiment, and the same was also used to generate the lookup table for estimation of the heat source intensity. The temperature and degree of cure for the lookup table ranged from T_1 = 265 K (-8.15 ^{o}C) to T_{max} = 400 K (125.85 ^{o}C) and φ_1 = 0.2 to φ_{max} = 1, respectively. θ_{mold} was set equal to the time history temperature data collected by the mold thermocouple referenced in Section 2.1.4.

A 4 x 401 nodal network was used for the state evolution model. A mesh convergence study was performed for the nodal network, and refinement beyond a 4 x 401 mesh did not provide significant improvement in the model accuracy. The locations of the rows of the FD nodal network within the domain and relative to the thermocouple locations are shown in Figure 2.10. The field of view of the IR camera did not encompass the entire length of the max chord, so only 356 of the 401 surface nodes (nodes lying on the top edge of the 2D slice) were used as measurement points. The camera had 1280 pixels in the length direction, so the temperature-time histories for the 356 measurement points were taken from the pixels which were closest to the evenly-spaced surface node locations. The locations of the four measurement points used for comparison to the estimation results are shown in Figure 2.10.

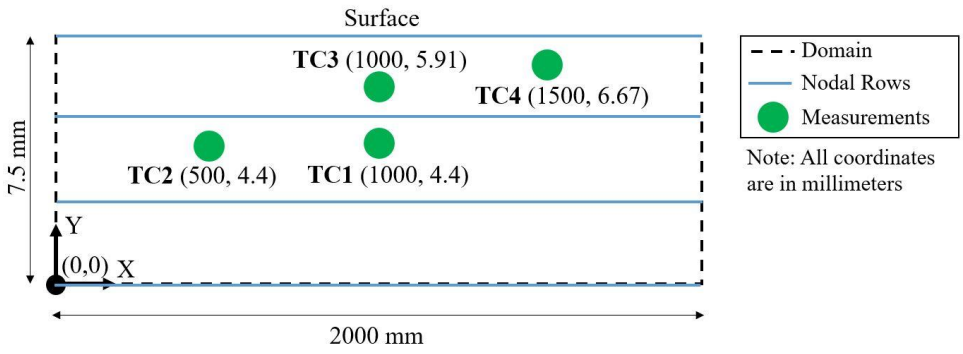

Figure 2. 10: Measurements and nodal network rows relative to approximate spar cap thickness. Note that the length and thickness of the part are not to scale in the figure.

As shown in Figure 2.10, the locations of the four embedded thermocouples do not coincide with the rows of the nodal network used in the state evolution model. In order to compare the results of the KF-based estimation method to measurements at those locations, the temperatures were approximated by linearly interpolating between the values of the nearest nodes directly above and below the thermocouples.

In the laboratory, the part was placed under vacuum for about 30 minutes before infusion without any heat input. As a result, the initial measured temperature of the part was assumed to be equal throughout the domain and was assumed to be equal to the temperature of the surrounding air. Therefore, the surrounding air temperature, θ_{surr}, and the initial temperatures, θ_{init} for each node in the network were all set equal to 20.87 °C, which was the average initial temperature measured by the IR camera. The initial standard deviation between all of the estimated temperatures was assumed to be small, at only 0.02 °C. In order to estimate the typical measurement error for the IR camera, the standard deviation in the IR camera measurements was computed separately from this experiment. 118 samples measuring the temperature of an object at room temperature were collected in time by the IR camera. The standard deviation of these measurements (σ_m) was computed and found to be 0.05 °C. This standard deviation was used to define the covariance matrix for the measurement error in the estimation method. σ_p was assumed to be 1.0 °C, approximately 20 times greater than σ_m. The estimated mean temperatures at the four measurement locations and the error between the estimates and the measured temperatures are shown in Figure 2.11. Standard deviation bounds of the mean +/- σ (estimated standard deviation) are also included. The degree of cure estimations over time are shown in Figure 2.12. The results are shown at the same locations as those shown in Figure 2.11. The root mean squared

(RMS) error between the estimated temperatures and the measured temperatures at the internal thermocouples during three different phases is shown in Table 2.2. These three phases are: pre-cure acceleration (Phase 1, 0 to 6000 s), temperature rise (Phase 2, 6000 s to 8000 s), and cooling (Phase 3, 8000 s to 11,220 s). Figure 2.12 shows that the estimated curing behavior matches well with the expected curing behavior for a resin used [47]. The reaction began to accelerate (Trommsdorff effect [79]) after about 6000 seconds, and within about 1000 to 2000 seconds after the acceleration, the resin was nearly completely cured.

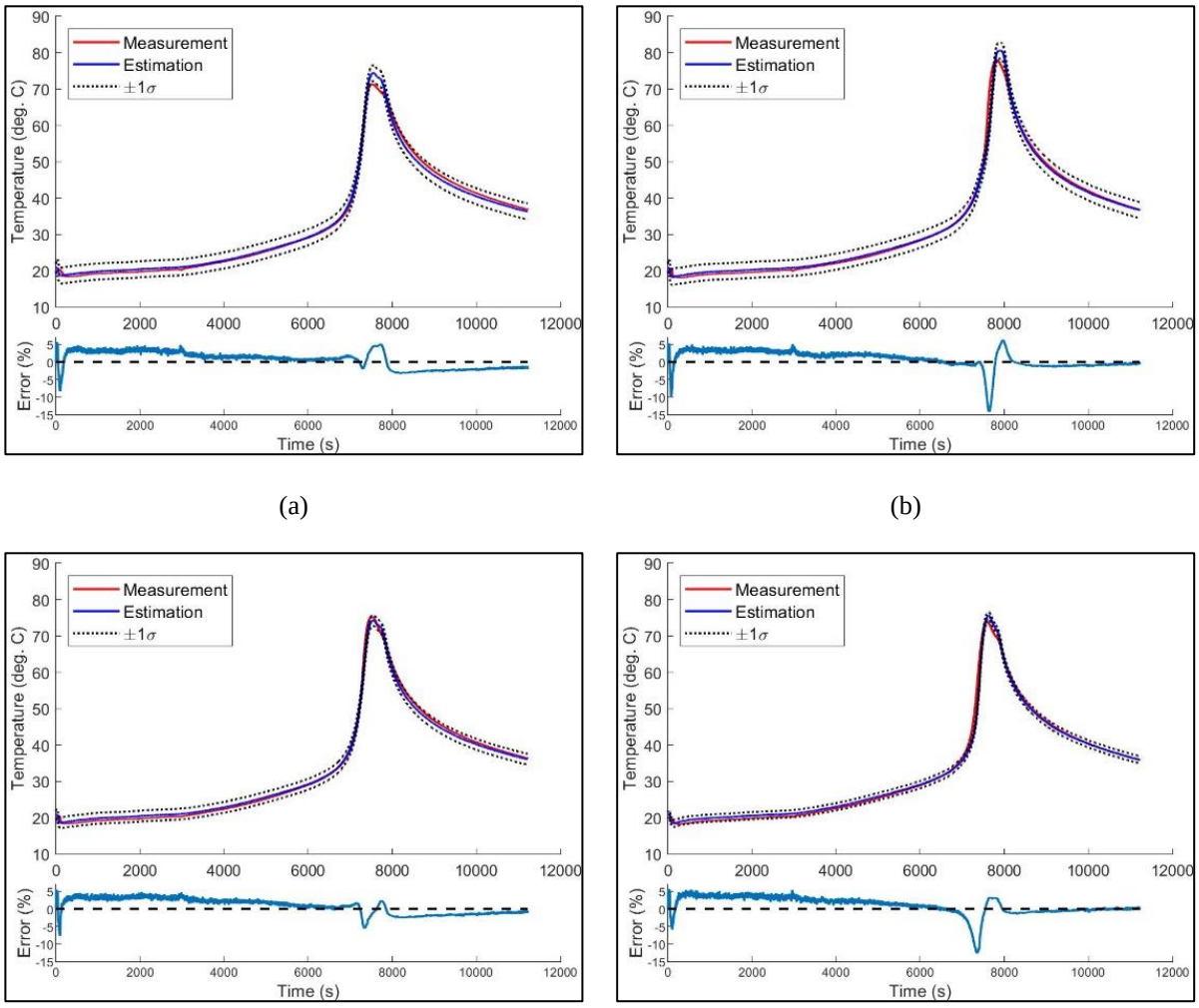

Figure 2. 11: Comparison of estimated mean temperatures and measured temperatures at a) TC1, b) TC2, c) TC3, and d) TC4 depicted in Figure 2.10

Table 2. 2: Root Mean Squared (RMS) error between the estimated and measured temperatures at all thermocouples during Phase 1, Phase 2, and Phase 3

RMSE (°C)	TC1	TC2	TC3	TC4
Phase 1	0.52	0.55	0.57	0.61
Phase 2	1.40	2.65	1.06	2.18
Phase 3	1.12	0.67	0.82	0.34

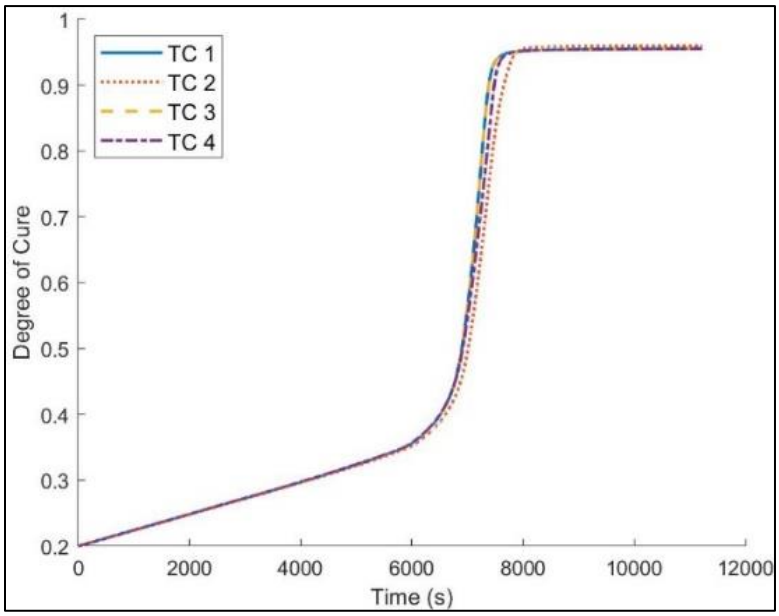

Figure 2. 12: Estimated Degrees of cure at the four thermocouple locations

As shown in Figure 2.11, the error in temperature estimation at times other than the peak was quite small for locations both close to the surface and deeper down, largely remaining below 5%. The errors at the peak were about 5% for all thermocouples, while the largest errors for the estimation occurred for thermocouples 2 and 4 during the temperature rise. At these locations, the estimated temperatures merely lag behind the measured temperatures by about 100 s during a period of rapid temperature increase. This lag and the slightly higher temperature reached at thermocouple 2 are both likely due to variations in the spatial distribution of resin between the different regions of the part (note the locations of thermocouples 2 and 4 in Figure 2.10). This can lead to differences in curing behavior between different regions, such as the times at which the Trommsdorff effect [47][79] initiates and the peak

temperatures that are reached. This is supported by the fact that cure acceleration occurred slightly later at the thermocouple 2 and 4 locations than for the other thermocouples, as shown in Figure 2.12. Additionally, as shown in Figure 2.13, the right side of the spar cap heats up sooner than the left side. The image in Figure 2.13 (a) was taken about 8 minutes before the image in Figure 2.13 (b). This potentially contributes to the estimation lagging behind the measured temperatures at these locations, as the cure acceleration in these regions (and as a result, the rate of temperature rise) would have been amplified by the higher temperatures in nearby regions that were further along in the curing process. Despite this, observing the rise periods of the temperature plots in Figure 2.11 qualitatively, it is clear that the estimation remains in good agreement with the measurements during the rise period, despite the lag.

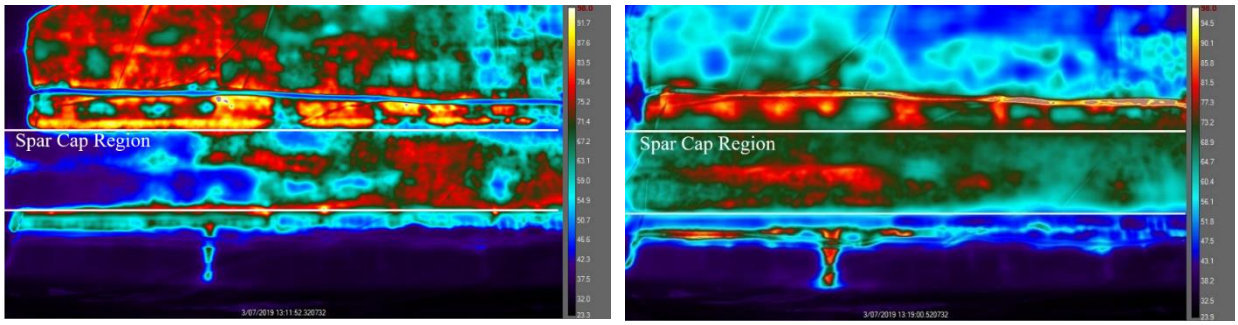

(a) (b)

Figure 2. 13: IR images showing the surface temperature distribution in the spar cap at 13:11 (a) and 13:19 (b). The temperatures on the right side of the images are in °C.

For the estimation results shown in Figure 2.11, the magnitude of the error increases sharply at the beginning, during the infusion period of the process. This is due to the resin cooling to below room temperature during the degassing process before infusion, which causes the part to cool during infusion. This cooling is not considered in the model. The standard deviation bounds in the thermocouple plots also show that the variance is greater at estimation locations further away from the surface. The higher variance deeper in the part is expected, since the information being fed to the KF is from the surface.

The ability to maintain accuracy despite the use of an approximate model for complex cure kinetics is a feature that has not been demonstrated in past temperature estimation studies for curing FRP composites. As shown in Table 2.2, the root mean squared (RMS) error between the estimated temperatures and the measured temperatures at the internal thermocouples remains below 3 °C for all four locations during the pre-cure acceleration (Phase 1, 0 to

6000 s), temperature rise (Phase 2, 6000 s to 8000 s), and cooling (Phase 3, 8000 s to 11,220 s) phases of the curing process. Crucially, the method was able to provide real-time estimations as well. It performed about 1.6 estimations per second (computation time of about 7000 seconds) on a personal computer with an Intel core i5 vPro processor, so it is fast enough to be performed in real time with data taken at 1 Hz. A direct comparison between the computational speed of this method with other temperature estimation techniques for curing composite materials is difficult, on account of the dearth of reported computational speeds of these other techniques in the literature. However, it is reasonable to expect execution of a KF-based method to be faster than those utilizing inverse methods, optimization-based solutions, or an Ensemble KF (discussed in Section 1). Thus, the cure monitoring methodology is likely the most suitable choice for performing real-time cure process monitoring with model-data fusion.

The accuracy of the temperature estimation, the capacity to perform real-time estimations for complex cure kinetics, and the ability to estimate the uncertainty in the temperature estimate using this technique all provide qualities for internal state estimation of FRP composites that are not currently found in previously-studied methods. Real-time estimation, the quantification of the uncertainty in the temperature estimation, and the estimation of degree of cure values can all be crucial features for adaptive decision making during and immediately after the manufacturing process.

2.3 Conclusions

In this chapter, a methodology was discussed for estimating both the internal temperatures as well as the degree of cure of a composite during the curing process using surface temperature measurements. A heat diffusion model for a curing composite and a KF-based temperature estimation method was implemented and validated using laboratory experiments. The technique was capable of real time cure monitoring, even for large parts, such as the wind turbine blade max chord section used in the validation experiment. Despite various simplifying approximations made in the model, the method was able to accurately estimate the internal temperatures. The error in mean estimated temperatures as compared to measured temperatures was less than 5% for all times not including the initial infusion period and the temperature rise. The estimated mean temperature at during the temperature rise experienced 5-15% errors at all thermocouple locations. To the best of authors' knowledge, this is the only study to date to discuss real-time monitoring for resin systems with complex free-radical polymerization reactions experiencing autoacceleration. Utilization of the true cure kinetics model for the resin used in the experiment to generate the simplified cure kinetics

model would likely improve the accuracy of the technique. Using models with higher fidelity (i.e. those that incorporate a more sophisticated cure kinetics model or the temperature- or cure-dependent variation in properties) would also improve accuracy (at the cost of the capability to perform real-time estimation).

Chapter 3. Flaw Detection in Curing Composites

The ultimate goal of the FRP composites work is not only to estimate internal temperatures in real-time, but also to identify flaws in an FRP composite from data measured during the curing process. This requires a non-destructive flaw identification technique with sufficient speed to identify flaws in real-time. The following sections detail a flaw detection method that utilizes the correction terms used in the temperature estimation technique described in the previous chapter. The goal is to verify whether the temperature estimation technique described in the previous chapter is capable of producing accurate estimates in the presence of flaws and whether the flaw detection method can accurately identify flaws. Despite the importance of the method's ability to perform real-time detection, this study will focus first on the technique's ability to accurately detect flaws. Three case studies are performed during the verification process for both the temperature estimation technique and the flaw detection method. The results of the verifications are presented and discussed in this chapter.

3.1 Methodology

In this section, a model of the governing physics of the heat diffusion in an FRP composite during the curing process is first described. This model is very similar to that which was used in the previous chapter, but a 3D domain is utilized instead of a 2D domain. A Kalman filter that fuses the information obtained from the assumed physics model (the state evolution model) and IR thermography data is utilized. A method for performing flaw detection in curing composites using the cumulative magnitudes of the corrections provided by the KF is discussed. The methodology of simulation-based case studies for the verification of the effectiveness of the flaw detection technique are described as well.

3.1.1 Computational Model of the Governing Physics

As was stated in Chapter 2, the heat transfer in the composite part is governed by the first law of thermodynamics. As with the model in Chapter 2, mass transfer is ignored and energy loss due to radiation is considered to be negligible. Additionally, the material is assumed to be homogeneous, and the heat conduction simulation is performed using *time-invariant*, *effective* thermal properties of the composite part. In contrast to the model described in Chapter 2, the domain is now hexahedral (3D), and the material is no longer modeled as isotropic. The 3D domain is shown in Figure 3.1.

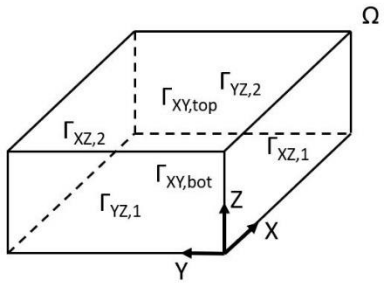

Figure 3. 1: 3D domain (Ω) used for computational model

The composite is assumed to be unidirectional (i.e. the fibers are all oriented in the same direction), and the differences in thermal conductivity between the longitudinal direction (the direction along the fiber direction) and the transverse directions are considered. The x-direction is chosen to be the longitudinal direction, while the y- and z-directions were chosen as the transverse directions. For unidirectional composites, the thermal conductivity in the longitudinal direction can be determined using the rule of mixtures, while the conductivities in the transverse directions can be determined using the inverse rule of mixtures [1]. The approximate upper and lower limits of volumetric properties, such as density and specific heat, can also be computed using the rule of mixtures and the inverse rule of mixtures, respectively. For the purposes of this study, the mean values of the upper and lower limits for the two properties can be used. The rule of mixtures equations used to compute the conductivities (and the upper and lower limits of the volumetric properties by substituting their respective values) are:

$$k_x = v_f k_f + (1 - v_f) k_m, \tag{3.1a}$$

$$k_{y,z} = \left(\frac{v_f}{k_f} + \frac{1 - v_f}{k_m} \right)^{-1}, \tag{3.1b}$$

where k_x is the thermal conductivity in the x-direction, $k_{y,z}$ is the thermal conductivity in the y and z (transverse) directions, v_f is the fiber-volume fraction, k_f is the thermal conductivity of the fiber material, and k_m is the thermal conductivity of the matrix material. As such, the thermal conductivity vector, $\boldsymbol{k}$, can be defined as $\{k_x, k_y, k_z\}$, and the governing equation stated in Equation 2.1 in Chapter 2 can be restated as:

$$\rho C_p \frac{\partial \theta(\boldsymbol{x}, t)}{\partial t} - \boldsymbol{\nabla} \cdot (\boldsymbol{k} \boldsymbol{\nabla} \theta(\boldsymbol{x}, t)) = f(\theta(\boldsymbol{x}, t), \varphi(\boldsymbol{x}, t)), \text{for } \boldsymbol{x} \in \Omega, \tag{3.2}$$

The initial and boundary conditions to which the governing equation is subjected are given by:

$$(k \boldsymbol{\nabla} \boldsymbol{\theta}) \cdot \boldsymbol{n} = h(\boldsymbol{\theta} - \theta_{surr} \cdot \boldsymbol{e}_{ID}), \text{for } \boldsymbol{x} \in \Gamma_{XY,1} \cup \Gamma_{XY,2} \cup \Gamma_{YZ,1} \cup \Gamma_{YZ,2} \cup \Gamma_{XZ,top}, \tag{3.3a}$$

$$(k \boldsymbol{\nabla} \boldsymbol{\theta}) \cdot \boldsymbol{n} = 0, \text{for } \boldsymbol{x} \in \Gamma_{XZ,bot}, \tag{3.3b}$$

$$\boldsymbol{\theta}(\boldsymbol{x}, 0) = \theta_{init} \cdot \boldsymbol{e}_{ID}, \forall\, \boldsymbol{x}. \tag{3.3c}$$

where θ_{surr} is the temperature of the surrounding air, θ_{init} is the initial temperature of the part, and h is the convective heat transfer coefficient. All boundaries aside from the bottom boundary in the XZ plane are convective boundaries with the surrounding air, while the bottom boundary is assumed to be insulated. As with the study performed in Chapter 2, the resin used for the studies in this article cures at room temperature, therefore the only heat input to the system comes from the exothermic reaction. The well-known, forward in time, centered in space (FTCS) finite difference approximation of the heat equation [2] is again used to discretize the governing equation to enable cure monitoring in near-real-time. The heat equation can be approximated using FTCS as follows,

$$\boldsymbol{\theta}^i = \boldsymbol{M} \boldsymbol{\theta}^{i-1} + \boldsymbol{b} + \frac{\Delta t}{\rho C_p} \boldsymbol{f}^{i-1}, \tag{3.4}$$

where $\boldsymbol{M}$ is the diffusivity matrix, $\boldsymbol{\theta}^i$ is the temperature vector containing the temperatures of all nodes at time step *i*, $\boldsymbol{b}$ is a vector containing boundary condition terms which are not related to the temperature states, $\boldsymbol{f}^{i-1}$ is the heat generation vector at time step *i-1*, and Δt is the time step used for the time marching scheme [2]. The same heat source model that was used in Chapter 2 is also used in Chapter 3. The heat generated by the resin and the rate of cure, are related by the following equation:

$$\boldsymbol{f}^{i-1} = (1 - v_f) H_{resin} \rho_{resin} \dot{\boldsymbol{\varphi}}^{i-1}(\boldsymbol{\theta}^{i-1}, \boldsymbol{\varphi}^{i-1}), \tag{3.5}$$

where H_{resin} is the heat of reaction for the resin, ρ_{resin} is the density of the resin, and v_f is the fiber-volume fraction [3]. The density of the resin was assumed to be constant and was provided to the authors by the resin manufacturer, as was the heat of reaction for the resin. The rate of cure vector, $\dot{\boldsymbol{\varphi}}^{i-1}$, can be determined using the look up table described in Chapter 2, and the degree of cure can be determined as discussed in Chapter 2. If the input vector, $\boldsymbol{u}^{i-1}$, is defined as

$$\boldsymbol{u}^{i-1} = \frac{\Delta t}{\rho C_p} \boldsymbol{f}^{i-1}, \tag{3.6}$$

then Equation 3.4 can then be expressed as:

$$\boldsymbol{\theta}^{i} = \boldsymbol{M}\boldsymbol{\theta}^{i-1} + \boldsymbol{b} + \boldsymbol{u}^{i-1}. \tag{3.7}$$

The discretized governing equation (Equation 3.7) is then used in the temperature and degree of cure estimation technique.

3.1.2 Kalman Filter-based Flaw Detection Technique

A Kalman Filter (KF) provides correction to state variable values predicted by an assumed (process) model. If these predicted values require a large amount of correction, then the assumed model does not accurately predict the true behavior of the physics involved. This would occur either if the model does not describe the expected physics well, or if the physics behave differently than expected. An example of the latter is a situation when flaws are present that cause the physics to behave out of the ordinary. Therefore, provided the model describes the expected physics well enough, the magnitude of correction the KF provides for a location in the domain can be used as an indicator for potential flaw formation.

Restating Equation 2.14 from Section 2, the corrected state variables output by the KF at time step *i*, $\boldsymbol{\mu}^i$, can be expressed as

$$\boldsymbol{\mu}^i = \hat{\boldsymbol{\mu}}^i + \boldsymbol{K}^i \boldsymbol{v}^i, \tag{3.8}$$

where $\hat{\boldsymbol{\mu}}^i$ are the state variables predicted by the assumed model, $\boldsymbol{K}^i$ is the Kalman Gain, and $\boldsymbol{v}^i$ is the vector of differences between the measured values of certain state variables and the predicted values of those state variables. The product, $\boldsymbol{K}^i \boldsymbol{v}^i$, will be referred to as the "correction term" for the remainder of this work and is a key component

for the proposed flaw detection methodology. This vector provides an additive correction to the model-predicted values at each of the FD nodes in the domain at the time step, i.

The "cumulative correction term" (CCT), to which it will be referred in this work, can be used as a metric for flaw detection. The term is defined as:

$$CCT = \sum_{i=1}^{n} \boldsymbol{K}^i \boldsymbol{v}^i , \tag{3.9}$$

where n is the number of samples solved-for by the KF-based estimator. A metric that utilizes the actual values of the correction terms rather than the magnitudes and is cumulative in nature should help in reducing the effect of measurement noise-induced correction.

Identification of which metric values correspond to flaw locations can be performed using outlier detection. One important note related to this is that the magnitudes of the correction terms will decrease through the depth of the composite part. This is due to the fact that the correction will be greater at the top surface due to the noise from the measurements. The impact of the noise will be reduced through the depth, as the material itself will serve as a filter of sorts to reduce high-frequency content during the diffusion of heat through the part. As a result, each N_x by N_y "slice" through the material, where N_j corresponds to the number of nodes along the jth direction in the FD grid, will need to be considered separately, otherwise the CCT values from the top surface would dominate. Both the mean and standard deviation of the collection of CCT values from each slice can be computed. Locations within a slice with CCT values greater than or less than three standard deviations from the mean value for that slice can be determined to be outlier locations and can therefore be deemed potential flaw locations.

A matrix, $\boldsymbol{M}$, with dimensions equal to N_x x N_y x N_z, can be formed, with each index corresponding to a nodal location. The matrix can be filled with 1's and 0's. Locations with a 1 are those with CCT values greater than or less than a certain number, n, of standard deviations (σ) from the mean, while locations with a 0 are not. In order to minimize the effect of noise, which is random, a median filter with a region of 3 nodes by 3 nodes can be applied to each slice of $\boldsymbol{M}$ along the z-direction (i.e. each N_x x N_y section of $\boldsymbol{M}$). The median filter changes the value of the central point in each 3x3 region to the median value of all points in that region. The central value of regions with few outliers

are thus changed to 0's, which, on account of the randomness of noise, eliminates outliers identified due to noise. The filtered, binary $\boldsymbol{M}$ matrix is the final identifier for potential flaw locations.

3.1.2 Verification of Temperature Estimation Technique in the Presence of Flaws

In order for the technique outlined in Section 3.1.1 to work effectively, the KF-based estimator must be able to accurately estimate temperatures in the presence of flaws. The model used for the estimator will have no knowledge of the size, location, or effect of a flaw, so the only information about the presence and location of the flaw comes from the measurement data. In order to show that the estimator can estimate temperatures accurately in the presence of flaws, a simulation-based verification study is performed. Simulation data is produced using the model that assumes there are not flaws, for comparison to the results that will include flaws. Simulation data can also be produced using a model that includes a flaw in the 3D domain. A flaw is introduced by changing the fiber-volume fraction in the flaw region, $v_{f,flaw}$, relative to the fiber-volume fraction of the rest of the domain, v_f. The data produced by this simulation represents the measured, real-life data from an actual part. The data from the top face nodes is then used as measurements for the KF-based estimator. Gaussian White Noise is added to the simulation data used as measurement data to simulate measurement noise.

The temperature and degree of cure time history results produced by the KF-based estimator using both a model that has no knowledge of the flaw(s) and the measurement data from the flawed simulation(s) is compared to the data from the simulation(s) with a flaw modeled at the selected nodes. Verification is deemed successful if there is relatively small error between the mean temperatures estimated by the KF-based estimator and the simulation data than there was between the temperatures predicted by the non-filtered model and the simulation data. Essentially, verification is successful if the KF-based estimator improves the accuracy of the assumed model using the measurement data.

3.1.3 Verification of Flaw Detection Technique

Once the temperature estimation technique's ability to improve the accuracy of the model estimates using measurement data is verified, the flaw detection technique's ability to accurately identify flaw locations can be

verified. The simulation data used for verification of the temperature estimation technique can also be used for verification of the flaw detection technique. The correction terms used by the estimation technique is recorded for all FD nodes and times, and the CCT is computed for all points. As described in section 3.1.2, locations that are outliers in terms of their CCT are determined to be probable flaw locations. Verification is deemed successful if the actual flaw locations (locations of the flaws in the simulation model) are correctly identified as likely flaw locations by the flaw detection technique.

In order to verify the generality of the accuracy of both the estimation technique and the flaw detection method in the presence of flaws, three case studies can be performed. All three case studies involve the use of an assumed model that has no knowledge of a flaw. The case studies are outlined below:

1. The assumed model has no knowledge of a flaw. The measurement data fed to the KF will be from a simulation with one flaw.
2. The assumed model has no knowledge of a flaw, and the assumed cure kinetics model is incorrect. The measurement data fed to the KF will be from a simulation with one flaw (the same data from Case 1).
3. The assumed model has no knowledge of a flaw. The measurement data fed to the KF will be from a simulation with two flaws.

3.2 Results and Discussion

3.2.1 Verification of Temperature Estimation Technique in the Presence of Flaws

The ability of the KF-based temperature estimation algorithm to improve the internal temperature estimates compared to that of an assumed simulation model was tested using simulation data. The chosen domain size was 0.1 m by 0.1 m by 0.02 m. A finite-difference network of 31x31x7 was chosen for this domain, and a time step of 5 seconds was used for the simulations. The fiber-volume fraction of the non-flawed region of the part was chosen to be 0.5. k_f was 1.3 W/mK, and k_m was 0.20 W/mK. ρ_f was 2500 kg/m^3, and ρ_m was 1200 kg/m^3. $C_{p,f}$ was 800 J/kgK, and $C_{p,m}$ was 1000 J/kgK. Using Equation 3.1 and selecting the mean values of the upper and lower bounds for the volumetric properties, k_x = 0.75 W/mK, $k_y = k_z$ = 0.35 W/mK, C_p = 894.4 J/kgK, and ρ = 1736 kg/m^3. The convection

coefficient was 5.6 W/m^{2}K. The heat generation model utilized the lookup table described in Chapter 2 as the cure kinetics model.

Two different cases were studied for this verification: one with $v_{f,flaw}$ = 0.1, and one with $v_{f,flaw}$ = 0.9. The flaws were 1 cm by 1 cm squares in the XY plane and were placed in the center of the domain in the XY plane. The flaws were located on the 4th and 5th surfaces through the thickness (with the 1st surface being the bottom XY surface of the FD network). Simulations were performed to produce measurement and verification data for both cases. Gaussian white noise with a standard deviation of 0.1°C was added to the measurement data to simulate the measurement data being collected by the IR camera used in Chapter 2. This measurement data was then used in conjunction with the KF-based estimator to produce estimates of the temperatures in the simulated curing composite part. The model assumed for the estimator had no knowledge of the flaws, i.e. the assumed fiber-volume fraction was equal to 0.5 for the entire domain. Any information about the flaws was only known via the measurement data. The results produced by the estimator for both cases were compared to simulation results of the unfiltered, assumed model to show that the KF-based estimator is able to improve the accuracy of the estimation in the presence of flaws. The results of the verification study are shown below in Figure 3.2. The comparison point for the verification is directly in the center of the part, which is where the flaw is located.

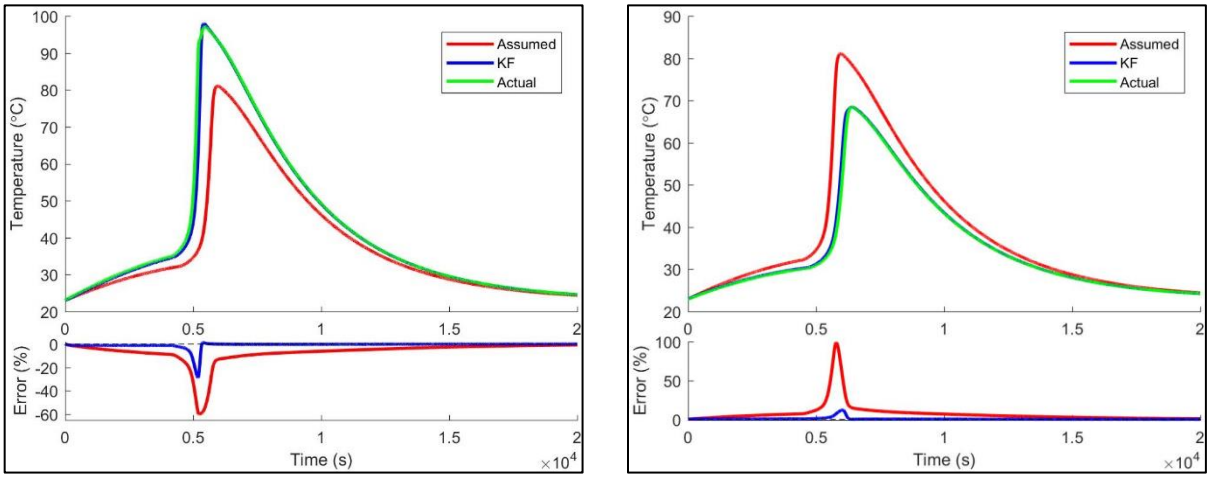

(a) (b)

Figure 3. 2: Comparison of estimated temperatures using the assumed model and the KF-based estimator for $v_{f,flaw}$ = 0.1 (a) and $v_{f,flaw}$ = 0.9 (b)

The results indicate that the KF-based estimator produces a greatly-improved temperature estimate at the flaw location over the model with no knowledge of the flaw. The maximum error for the assumed model was about 60% for $v_{f,flaw}$ = 0.1 and 100% for $v_{f,flaw}$ = 0.9, while the error reduced to about 27% and 12%, respectively, with the correction applied by the KF-based estimator. Qualitatively, the estimates produced by the KF-based estimator show a better match with the true process state values than do the predictions of the assumed model. The correction at this location was large, and this will be captured by the CCT value that is computed for the flaw detection method. Therefore, the results of this verification study are promising for the evaluation of the flaw detection method.

3.2.2 Verification of Flaw Detection Technique

Next, the performance of the flaw detection method itself was evaluated using simulation data. The domain, finite-difference network, time step, and material properties used for these simulations were the same as those used for the verification study performed in Section 3.2.1.

For Case Studies 1 and 2, flaws were 1 cm by 1 cm squares in the XY plane and were placed in the center of the domain in the XY plane. The flaws were located on the 4th and 5th surfaces through the thickness (with the 1st surface being the bottom XY surface of the FD network). For each of the Studies, simulation data was produced for cases with $v_{f,flaw}$ = 0.1 up to $v_{f,flaw}$ = 0.9, in steps of 0.1. As with the verification study in Section 3.2.1, Gaussian White Noise with a standard deviation of 0.1°C was added to the simulation data used as measurement data, which is a typical amount for measurements being collected with an IR camera. The measurement data for each case was utilized, along with a KF, to correct the temperature predictions of the assumed model with no knowledge of the flaws. The CCT was computed for each case, and subsequently, the outlier nodes were determined, as described in Section 3.1.2. A criterion of 3σ was used for the outlier detection, meaning only locations with CCT values greater or less than three standard deviations from the mean CCT value for their particular surface in the XY plane were chosen as outliers. This strict criterion was chosen in order to potentially reduce the number of false positives for the flaw detection. The locations of the outlier nodes, if any were identified, were then compared to the locations of the actual flaws to verify that the locations matched. Images of the outlier maps for surfaces 4 and 5 for a case of $v_{f,flaw}$ = 0.1 are shown in Figure 3.3. The regions of the surface identified as flaws are highlighted in red, while regions without identified flaws are highlighted in blue. As shown in the maps, the flaw (located in the centers of surfaces 4 and 5) was detected.

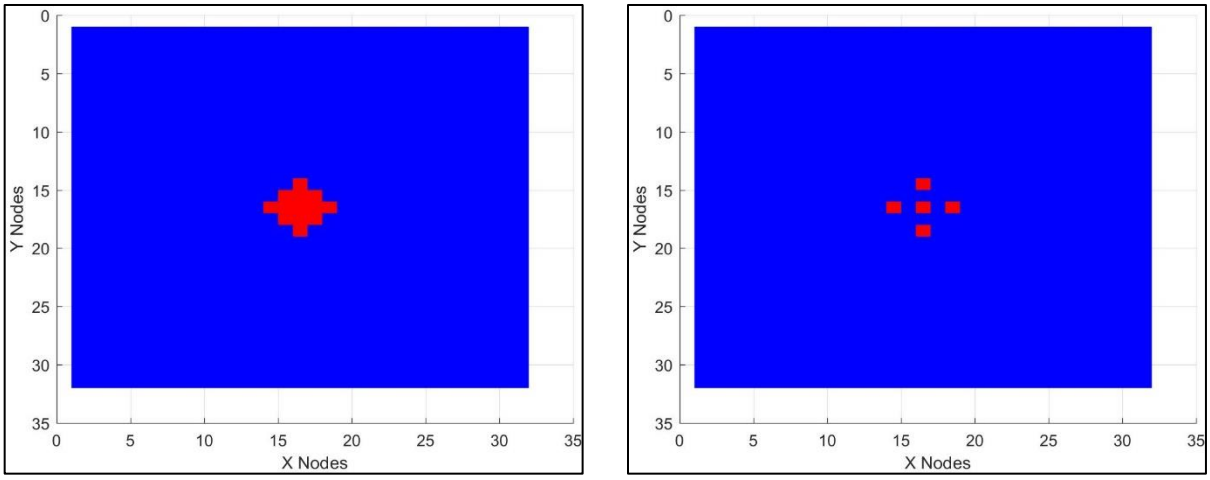

(a) (b)

Figure 3. 3: Outlier maps for surfaces 4 (a) and 5 (b) for $v_{f,flaw}$ = 0.1

Full results for Case Studies 1 and 3 when using a 3σ criteria are shown in Table 3.1. If the technique correctly identified the flaw region, then the case was assigned a "correct" description in the table, and if the technique did not correctly identify the flaw region, then the case was assigned an "incorrect" description in the table. Additionally, the descriptive label "FP" was used to identify situations when the technique incorrectly identifies a region as a flaw (false positive). For example, the technique may correctly identify a flaw region while also producing a false positive in another region. In that case, the description would read "correct, FP". The "correct" descriptions are also highlighted in green, while the "incorrect" descriptions and the false positive descriptor are highlighted in red. Cases marked with a red asterisk were cases for which flaws were identified using n = 2.8 but not for n = 3.

Table 3. 1: Results of Flaw Detection for Case Studies 1 and 2. Cases marked with a * indicate that the flaw was detected for n = 2.8 but not for n = 3

$v_{f,flaw}$	Study 1	Study 2
0.1	Correct	Correct
0.2	Correct	Correct
0.3	Correct	Correct
0.4	Correct	Correct
No Flaw	Correct	Incorrect, FP
0.6	Correct	Correct*
0.7	Correct	Correct
0.8	Correct*	Correct*
0.9	Correct*	Correct*

The results of the Case Studies 1 and 2 indicate that the technique performs very well when identifying resin-rich regions (low fiber-volume fraction), while identification of dry regions (high fiber-volume fraction) required a slightly less-strict outlier criterion (n = 2.8 as opposed to n = 3). The incorrectly-assumed cure kinetics model utilized for Case Study 2 did not appear to affect the results of the resin-rich flaw identifications, but extent of the flaw was identified in this Study was smaller compared to Case Study 1. A false positive was also produced for the non-flawed case in Case Study 2, which was small and occurred in an innocuous location somewhat close to the right boundary of the XY plane. The non-symmetry and random location of false positive indicates that the occurrence is due to the magnitude of the noise correction in that region relative to others, and not due to the correction related to the erroneous model. While such false positives are possible when using this technique, utilizing a low-pass filter or some other means of noise reduction for the measurement data would reduce the chances of false positives occurring. Implementation of a low-pass filter for real-time measurement would likely require the measurement data to pass through an electrical filtering circuit or a digital filter (rather than applying the low-pass filter to the data once all data had been collected), but it is a realistic approach.

For Study 3, two flaws were placed in the part. The flaw locations for Study 3 are shown in the XZ plane in Figure 3.4.

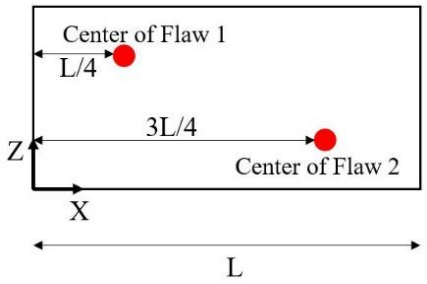

Figure 3. 4: Diagram showing the locations of the centers of the two flaws for Case Study 3

Flaw 1 was located closer to the top surface, on the 5th and 6th surfaces through the thickness, while Flaw 2 was located deeper in the part, on the 2nd and 3rd surfaces. The reasoning for studying this particular situation is to observe whether the deeper flaw is able to be identified by the technique, even if a different flaw, closer to the measurement surface, is present. Only three specific cases were tested for Study 3. For the first, both Flaw 1 and Flaw 2 had fiber-volume fractions of 0.2. For the second, Flaws 1 and 2 had fiber volume fractions of 0.2 and 0.6, respectively. For the third, Flaws 1 and 2 had fiber-volume fractions of 0.6 and 0.2, respectively. The reasoning for studying these particular cases was to study a case where the both the near-surface and deep flaws were strong flaws (i.e. having a fiber-volume fraction deviating from 0.5 by a large amount) (Case 1), a case where the deeper flaw was weaker (Case 2), and a case where the deeper flaw was stronger (Case 3). For each of the three cases, the two flaws were both 1 cm by 1 cm in the XY plane. Results showing whether each flaw was detected or not for the three cases are shown in Table 3.2. Similar to Table 3.1, flaws that were “detected” are highlighted in green, while flaws that were not are highlighted in red.

Table 3. 2: Results of Flaw Detection for Case Study 3 when using 3σ criteria

Case	Flaw 1	Flaw 2
$\boldsymbol{v_{f,flaw1} = 0.2, v_{f,flaw2} = 0.2}$	Detected	Not Detected
$\boldsymbol{v_{f,flaw1} = 0.2, v_{f,flaw2} = 0.6}$	Detected	Not Detected
$\boldsymbol{v_{f,flaw1} = 0.6, v_{f,flaw2} = 0.2}$	Detected	Detected

The results show that when there are multiple flaws present, the technique is more likely to identify the flaw that is closer to the measurement surface than the flaw that is deeper in the part. In order for the deeper flaw to be identified in the presence of a near-surface flaw, the flaw must be fairly significant relative to the near-surface flaw. The inability to detect deeper flaws when a strong surface flaw is present is not a significant detriment to the technique's usefulness in the field. The goal of this technique is to identify potential flaws during cure to inform decision making in regards to post-manufacturing inspection. This means that if no flaws are detected by the method during manufacturing, post-manufacturing inspection can be performed, with the goal being to reduce the overall inspection time. However, if any flaw is detected, such as a strong near-surface flaw, this would likely prompt a more thorough post-manufacturing inspection of the part. Such an inspection could then uncover the presence of the deeper flaw as well.

Each run of the flaw detection method, including the Kalman-filtered based estimation in the 3D domain, the evaluation of the CCT values, and the determination of outliers, required approximately 8 hours. Almost all of this time was spent performing the KF-based estimation. In order for the technique described in the Chapter to be of use for real-time cure monitoring, the computational efficiency of the technique will need to be improved, particularly if the technique is applied to larger composites.

3.3 Conclusions

In this chapter, a technique for detecting flaws in FRP composites during the curing process using IR thermography measurements, the temperature estimation method described in Chapter 2, and the CCT (a metric computed from the Kalman filter corrections) was described. The ability of the temperature estimation technique to improve temperature estimation accuracy in the presence of flaws was verified using simulation-based data. The flaw

detection method's effectiveness was also evaluated using simulation-based verification case studies. The method showed the ability to identify resin-rich areas of an FRP composite very well, but identification of resin-deficient regions internal to the part required a slightly less-strict outlier criterion. An incorrectly-assumed model was utilized as the base heat conduction model for Case Study 2, and the technique was still able to detect the presence of the flaw in resin-rich cases. One false positive was also produced for a non-flawed case, but this issue can likely be solved with the use of noise-reduction measures. The technique's ability to identify multiple flaws was also evaluated. When both a near-surface and deep flaw were present, the technique only identified the near-surface flaw, unless the deeper flaw resulted in significant deviation from the expected behavior than the near-surface flaw. This would not be an inhibition to implementing this technique in an industrial setting, however, as the identification of one flaw would indicate that the part should be thoroughly evaluated in post-manufacturing inspection. The deeper flaw would be captured by this thorough inspection.

Chapter 4. Corrosion Detection in Nuclear Power Plant Pipes

In this chapter, an NDE method for detecting wall thinning resulting from flow-accelerated corrosion (FAC) in nuclear power plant pipes is described. First, the details of methodology and the simulations used for verification are discussed. The results of the verification study are then presented and discussed, followed by conclusions.

4.1 Methodology

In this section, two models for the governing physics of heat diffusion through an insulated carbon steel pipe are first discussed. The wall thickness estimation technique is then described. The technique utilizes a surrogate (GPR) model that estimates wall thickness for a pipe based on the change in measured steady-state temperature between the initial and the current state (wall thickness) of the pipe. These measurements would be collected using thermocouples attached to the outside of the pipe in practice, but the focus here is on proving out the estimation methodology using simulations. Lastly, the methodology is verified using numerical experiments.

4.1.1 Model of Governing Physics

Two different mathematical models can be utilized to describe the physics of the heat transfer through an insulated pipe. One model includes the effect of the layer of insulation surrounding the pipe directly, while the other model approximates the effects of the insulation. While both models will be described, the approximate model will be utilized for future analyses. For both models, a two-dimensional, circular cross-section of a pipe is considered, with water flowing in the direction normal to the plane of the paper. Heat flows from the water, through the pipe, and to the surrounding air outside the pipe, due to the water having a higher temperature than the surrounding air. The heat equation governs the heat transfer inside the pipe wall. Given that the domain is a circular cross-section, polar coordinates are well-suited for the mathematical model. A diagram showing the 2D domain including the insulation is shown in Figure 4.1(a). This domain is that which would be used for the first model. The cross-section has an inner radius of r_i, and an outer radius of r_o. A layer of insulation with thickness d_{ins} surrounds the pipe on the outside. The

domain utilized for approximate model is shown in Figure 4.1(b). This domain only consists of the metallic pipe, and the model utilizes an approximate convective boundary condition to account for the effect of the insulation. When a domain discretization method is used to solve the governing equations numerically, the approximate model incurs lower computation cost as compared to the model that explicitly considers the insulation. The approximate model is used for performing the simulations required for both the implementation and verification of the technique.

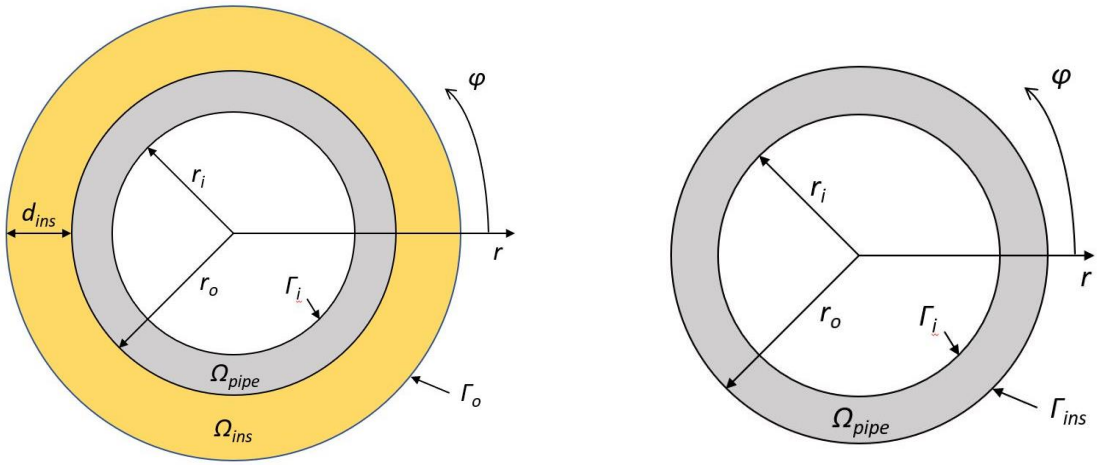

(a) (b)

Figure 4. 1: Diagram of 2D pipe domain with (a) and without insulation (b)

The metallic pipe has a thermal conductivity of k_{pipe}, a density of ρ_{pipe}, and a specific heat of $C_{p,pipe}$, while the insulation has properties of k_{ins}, ρ_{ins}, and $C_{p,ins}$. The heat equation in polar coordinates, where $\boldsymbol{r} = \{r, \varphi\}$, can be expressed for both the metallic pipe region of the domain (Ω_{pipe}) and the insulation region of the domain (Ω_{ins}) as:

$$\rho_{pipe} C_{p,pipe} \frac{\partial \theta(\boldsymbol{r},t)}{\partial t} - k_{pipe}\left[\frac{1}{r}\left(\frac{\partial \theta(\boldsymbol{r},t)}{\partial r} + r\frac{\partial^2 \theta(\boldsymbol{r},t)}{\partial r^2}\right) + \frac{1}{r^2}\frac{\partial^2 \theta(\boldsymbol{r},t)}{\partial \varphi^2}\right] = 0, \text{for } \boldsymbol{r} \in \Omega_{pipe}, \quad (4.1a)$$

$$\rho_{ins} C_{p,ins} \frac{\partial \theta(\boldsymbol{r},t)}{\partial t} - k_{ins}\left[\frac{1}{r}\left(\frac{\partial \theta(\boldsymbol{r},t)}{\partial r} + r\frac{\partial^2 \theta(\boldsymbol{r},t)}{\partial r^2}\right) + \frac{1}{r^2}\frac{\partial^2 \theta(\boldsymbol{r},t)}{\partial \varphi^2}\right] = 0, \text{for } \boldsymbol{r} \in \Omega_{ins}, \quad (4.1b)$$

The initial and boundary conditions for the first model are given by:

$$(k\boldsymbol{\nabla\theta})\cdot\boldsymbol{n} = h_i(\boldsymbol{\theta}-\theta_w\cdot\boldsymbol{e}_{ID}), \text{for } \boldsymbol{r}\in\Gamma_i, \tag{4.2a}$$

$$(k\boldsymbol{\nabla\theta})\cdot\boldsymbol{n} = h_o(\boldsymbol{\theta}-\theta_{surr}\cdot\boldsymbol{e}_{ID}), \text{for } \boldsymbol{r}\in\Gamma_o, \tag{4.2b}$$

$$\boldsymbol{\theta}(\boldsymbol{r},0) = \theta_{init}\cdot\boldsymbol{e}_{ID}, \forall\,\boldsymbol{r}. \tag{4.2c}$$

where $\boldsymbol{e}_{ID}$ is a vector of ones with the same length as $\boldsymbol{\theta}$. The convective heat transfer coefficient at the boundary between the insulation and the surrounding air is h_o. The convective heat transfer coefficient at the boundary between the pipe and the water is h_i. The boundary conditions for the second model are slightly different, due to the convective-boundary approximation of insulation. The boundary condition at the inner boundary remains the same, and the boundary conditions at Γ_{ins} is given by:

$$(k\boldsymbol{\nabla\theta})\cdot\boldsymbol{n} = h_{ins}(\boldsymbol{\theta}-\theta_{surr}\cdot\boldsymbol{e}_{ID}), \text{for } \boldsymbol{r}\in\Gamma_{ins}. \tag{4.2d}$$

This boundary condition combines the effects of the conductive heat transfer through the insulation and the convective heat transfer between the insulation and the surrounding air. The heat transfer coefficient, h_{ins}, can be approximated via a parameter estimation method that minimizes the difference between the temperature output of the model that does include the insulation and the approximate model that does not.

The value of the internal convection coefficient, h_i, can be approximated using an empirical relationship between convective heat transfer and characteristics of the flow in a circular pipe. Determination of which empirical relationship is most applicable depends on the dimensionless quantities, the Reynolds number (*Re*) and the Prandtl number (*Pr*). The simplest of these correlations for turbulent flow is:

$$Nu_D = 0.023{Re_D}^{4/5}Pr^n, \tag{4.3}$$

where Nu_D is the Nusselt number and Re_D is the Reynolds number. The exponent, *n*, has a value of 0.3 if the temperature of the pipe is greater than the temperature of the water, and it has a value of 0.4 if the temperature of the water is greater than the temperature of the pipe [76]. This correlation applies for smooth pipes, so although the inside surface of the pipe has roughness, its effect on the convection will be ignored. The convective heat transfer coefficient can be approximated with this correlation by using the definitions of the dimensionless quantities, the Nusselt number, and the Reynolds number, which are defined in Equation 4.4.

$$Nu_D \equiv \frac{h_i D}{k_w}, \tag{4.4a}$$

$$Re_D \equiv \frac{\rho_w u D}{\mu}, \tag{4.4b}$$

where D is the inner diameter of the pipe, k_w is the thermal conductivity of the water, ρ_w is the density of the water, μ is the dynamic viscosity of water, and u is the mean water speed through the cross-sectional plane. These properties (excluding the water speed), as well as the Prandtl number, can be determined based on the temperature of the water and the pressure in the pipe [76]. Substituting Equation 4.4 into Equation 4.3 and rearranging, the following expression is achieved:

$$h_i = \frac{0.023 k_w \rho_w^{4/5} Pr^n}{D^{1/5} \mu^{4/5}} u^{4/5}. \tag{4.5}$$

4.1.2 Corrosion Detection Technique

As described in Section 1.4, the utility of detecting wall thinning in pipes based on steady-state temperature measurements has not been studied previously. Thermocouples mounted to the outside of the pipe are an easy-to-use and cost-effective measurement method for this purpose. In addition, the utilization of these thermocouples would not require the removal of insulation from the pipe, and the steady-state temperatures can be measured passively at any time during plant operation due to the natural heat transfer occurring in the pipe.

Differences in the steady state temperature of a pipe over time can be an indication of a number of changes, including a change in water temperature, water speed (which affects the inner convection coefficient), and surrounding air temperature. FAC-related features can also cause a change in steady-state temperature, such as the change in wall thickness. However, variables such as water temperature, water speed, or surrounding air temperature can be assumed to follow a Normal distribution, so the effect of variations in these three variables would, in turn, only produce fluctuations in the steady-state temperature around a mean value as well. The change in wall thickness is a permanent change in the geometry of the pipe that produces a shift in the mean steady-state temperature. Therefore, the *change* in mean steady-state temperature from the initial temperature taken at the original wall thickness and the mean steady-state temperature at a future time after corrosion had occurred, can be related to the change in wall thickness.

A model can be established to estimate wall thickness change using the change in steady-state temperature as an input using a Gaussian Process Regression (GPR) model. A GPR model is utilized due to the fact that the functional form of the model for the relationship between wall thickness change and the change in steady-state temperature is not known, and GPR is a nonparametric method (i.e. the method is not limited to a single, user-defined functional form). Training data for the GPR model can be produced using simulations of the heat transfer through the pipe to establish the change in steady-state temperature for various wall thickness values. Expected values for the parameters of the model, such as water temperature, water speed, pipe properties, and insulation properties can be used for the simulations.

Pipe fittings, like elbows, are an ideal candidate for application of this technique both due to the fact that they are highly susceptible to FAC (along with pipe section immediately following elbows) and they consistently show wall thinning at the outer bend of the elbow [65]. The knowledge of the location where the most wall thinning will occur around the circumference would ideally require the placement of only a single thermocouple at that circumferential location for monitoring.

4.1.3 Numerical Experiments

4.1.3.1 Estimation of Heat Transfer Coefficient

The heat transfer coefficient used to approximate the heat flow through the insulation, h_{ins}, can be determined using parameter estimation. Simulations of the heat transfer in a domain composed of the pipe, the surrounding insulation, and the internally-flowing water can be performed for various combinations of surrounding air temperatures, while maintaining the same water temperature. These simulations do not include thickness reductions. The temperature time histories produced by these simulations at the outer radius of the pipe can then be used as the target results for the optimization. A 1D FTCS model of the pipe can be used to approximate the heat transfer physics of the insulated model, including the approximated boundary condition described by Equation 4.2(d). Though this equation is presented for a 2D domain, the circumferential aspect can be ignored for this study, since there would be no heat transfer in the circumferential direction without a thickness reduction.

An optimization technique can be used to minimize the difference between the results of each simulation that includes insulation and the corresponding non-insulated simulation by adjusting the h_{ins} parameter value for each. The mean of the h_{ins} values produced for each of the cases can be used as the value for the approximation of the insulation's behavior.

4.1.3.2 Sensitivity Analysis

In order to establish the significance of variations in model parameters on the steady-state temperature, a sensitivity analysis can be performed. This analysis is necessary in order to decide the set of parameters to be used to generate simulation-based training data is sufficient. That is, the sensitivity analysis helps determine model parameters that significantly affect the output of the model (quantity of interest). The steady-state temperature at the outer radius of the pipe, which is where the measurement thermocouple would be placed, can be used as the output. Pipe thickness, thermal conductivity, density, specific heat, inner convection coefficient, external heat transfer coefficient, water temperature, and surrounding air temperature are the candidate model parameters.

A variance-based sensitivity analysis can be performed using Sobol indices as metrics for the significance of each parameter. The first-order Sobol index is indicative of the relative effect of the variations in each parameter on the variance of the output (the steady-state temperature) individually, while the Total Effect Sobol index also accounts for the interactions between the parameters. The first order index is defined as:

$$S_i = \frac{V_i}{Var(Y)},$$

where S_i is the first-order index for the *i*th parameter, $Var(Y)$ is the variance in the output, *Y*, and V_i is the variance in the expected value of the output with respect to the *i*th parameter. The total effect index is defined as:

$$S_{T,i} = \frac{E_{X_{\sim i}}(Var_{X_i}(Y|X_{\sim i}))}{Var(Y)},$$

where $S_{T,i}$ is the total effect index for the *i*th parameter and X_i is the *i*th parameter. Both the first order and total effect indices can be estimated using the quasi-Monte Carlo method [80][81]. A 1D forward in time, centered in space (FTCS) model for heat conduction can be utilized to produce simulation data for each parameter sample.

4.1.3.3 Verification of Gaussian Process Regression Models

Simulation-based verification studies is performed to determine the effectiveness of the method discussed in this chapter. Two different GPR models are analyzed, one that only uses the change in steady-state temperature from the initial steady-state temperature as an input (GPM1) and one that uses both water temperature and the change in steady-state temperature (GPM2). These two models are analyzed in order to determine the effectiveness of the method with and without knowledge of the current mean water temperature. Note that the training data for both GPR models was produced using the approximate model of the governing physics described in Section 4.1.1.

First, training data can be produced for a range of water temperature and wall thickness reduction values using simulations of the heat transfer physics described by Equations 4.1 and 4.2. An expected value for the water temperature can be chosen, and the training data can be produced for a range of water temperature values within a chosen deviation range. The thickness reduction values can range from zero to a value that is fairly close to the actual thickness of the pipe. For example, pipe ruptures have been reported for thicknesses of about 0.4 to 1.4 mm [60]. The change in steady-state temperature at the thermocouple measurement location (shown in Figure 4.2) from the zero-thickness reduction case can then be computed for all other thickness reductions for each water temperature. GPM1 and GPM2 can then be trained for the thickness reduction values for their respective input(s).

The thickness reduction for a pipe elbow cannot be considered to be uniform around the circumference, given that FAC has the largest effect at the outer curve of the pipe. Instead, the geometry of the thickness reduction can be assumed to follow a semi-elliptical path through the pipe material on only one side of the pipe (assumed to be the outer curve), as shown in Figure 4.2, where the cross-section has an inner radius of r_i, and an outer radius of r_o. r_{red} is the long-side radius of the half ellipse and corresponds to the radius at the point of greatest reduction (assumed to be directly in-line with the thermocouple along the outer curve of the pipe). Any pipe material between the half-elliptical

path and the original inner boundary is removed. Any wall thickness changes for the other side of the pipe (assumed to be the inner curve) are neglected. The thermocouple measurement location is labeled in the Figures as “TC”.

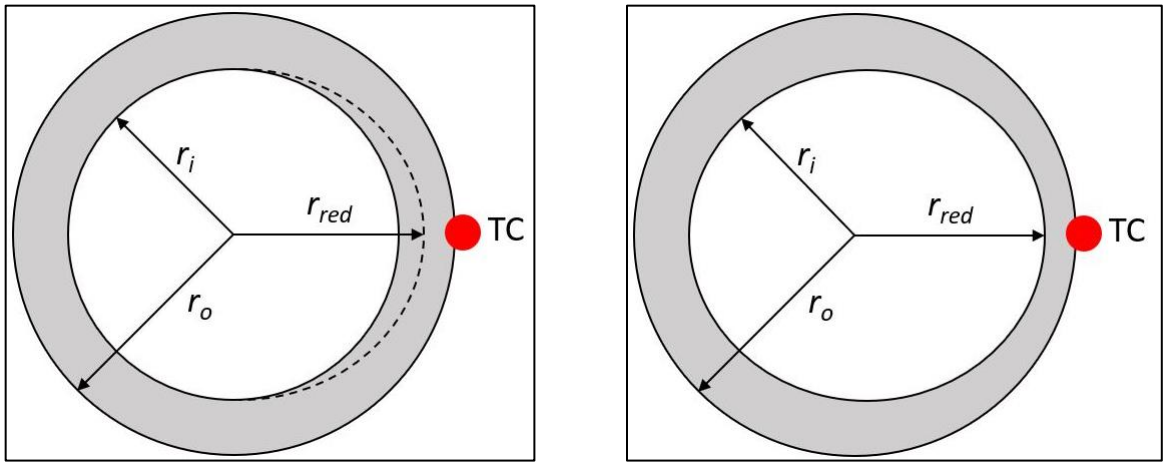

(a) (b)

Figure 4. 2: Diagrams of the pipe geometry before (a) and after (b) reduction of thickness. The thermocouple measurement location is denoted as “TC”

Testing data is produced for the purpose of verifying the accuracy of both of the GPR models. Simulation data can be produced for thickness reduction values that had not been trained. Additionally, the parameters of the model discussed for the sensitivity analysis, including water temperature, are all allowed to vary by up to 10% from the expected values used to produce the training data. Random combinations of the thickness reductions and parameter values are produced, and simulations are performed to determine the steady-state temperatures for the test data. Two simulations should be performed for each combination. For the first simulation, the varied parameter values can be used, but the thickness reduction is set to zero. The second simulation can utilize the varied thickness reduction value as well. The change in the steady-state temperature between the “current” thickness reduction and the initial thickness reduction are then computed by determining the difference in steady-state temperatures between the second and first simulations. The steady-state temperatures are then fed to GPM1 and GPM2 (along with the known water temperature for GPM2) and the resulting thickness reduction estimates can be compared to the true values for the testing cases for verification.

4.2 Results and Discussion

4.2.1 Estimation of Heat Transfer Coefficient

Simulations of an insulated pipe were performed in a 2D domain using the simulation software, ABAQUS [82]. The insulation properties, k_{ins}, ρ_{ins}, and $C_{p,ins}$ were defined as 0.05 W/mK, 80.1 kg/m^3, and 700 J/kgK, respectively, and the insulation thickness was defined as 3.81 cm. The inner radius of the pipe, r_i, and the outer radius of the pipe, r_o, were defined to be 24.6 and 30.2 mm, respectively. The values of the pipe properties, k_{pipe}, ρ_{pipe}, and $C_{p,pipe}$, were defined as 15.0 W/mK, 7850 kg/m^3, and 600 J/kgK, respectively.

The mean water speed was chosen to be 2.8 m/s and was used to approximate the expected value for the internal convection coefficient, h_i, as described in Section 4.1.1 (Equations 4.3 through 4.5). The value of this coefficient was determined to be 59 W/m^{2}K. As described in Section 4.1.3.1, the surrounding air temperature was varied from 0°C to 100°C in steps of 10°C for the eleven simulations used to produce the target data, while the water temperature was kept constant at 55°C for all simulations. 12.81 W/m^{2}K was found to be the value of h_{ins} that best fit the simulation data produced using the model with the fully-insulated domain, regardless of the surrounding air temperature value. The implementation of this approximation for the heat transfer of the insulation significantly reduces the computation time of subsequent ABAQUS simulations by reducing the size of problem domain.

4.2.2 Sensitivity Analysis

The sensitivity analysis was performed for 100,000 samples and all eight parameters. The parameter values assumed for the model described in Section 4.2.1 were used as mean values, and each parameter was allowed to vary by ±10%. The steady-temperature values produced by all of the simulations were used to compute the Sobol indices. The results are shown in Table 4.1. Higher values indicate higher relative influence and lower values indicate a lower relative influence.

Table 4. 1: Values of the Sobol indices for each parameter: Pipe thickness, thermal conductivity (k), density (ρ), specific heat (C_p), inner convection coefficient (h_i), external heat transfer coefficient (h_{ins}), water temperature (T_w), and surrounding air temperature (T_{surr})

Parameter	Thickness	k	ρ	C_p	h_i	h_{ins}	T_w	T_{surr}
S_i	0.02	~0	~0	~0	0.02	0.02	0.94	~0
$S_{t,i}$	0.02	~0	~0	~0	0.02	0.02	0.94	~0

The results of the sensitivity analysis indicate that the only parameter whose variation has a significant impact on the variation in the steady-state temperature is the water temperature. This is significant, as training data need not be reproduced for each individual instance of pipe sections with these same conditions. This also indicates that variations in water temperature can have a relatively significant impact on the steady-state temperature. As such, including the water temperature as an input to the estimation model is an option that should be explored.

It should be noted that although these results seem to indicate that the steady-state temperature is not a good metric for the identification of changes in wall thickness, this is not the case. As was noted in section 4.1.2, the *change* in steady-state temperature after installation of the pipe is more sensitive to the change in wall thickness, due to the fact that wall thickness is the only parameter that has an effect on shifting the mean value of the steady-state temperature over time. It should also be noted that a simplified 1D model was used to perform the sensitivity analysis. Reducing the thickness of the pipe in the 1D model is different from reducing the thickness for the 2D model used for verification, as the thickness is not uniformly changed for the 2D model.

4.2.3 Verification of Gaussian Process Regression Models

As described in section 4.1.3.3, training data for the GPR estimation model was produced using simulations performed in the ABAQUS simulation software [82]. The values of the parameters of the model used for the training data were the same as those chosen in section 4.2.1. As determined in Section 4.2.1, the chosen value for the external heat transfer coefficient was 12.81 W/m^{2}K. Training simulations were performed assuming an expected water

temperature of 80°C. Data was produced for water temperatures of 72°C to 88°C (a 10% variation from the expected value) and for thickness reductions from 0 mm to 4.5 mm in steps of 0.25 mm (for a 5.5 mm thick pipe). The simulation data for the 80°C simulations and all thickness reductions was used to train GPM1, while the simulation data for all temperatures and thickness reductions was used to train GPM2. The change in steady-state temperature for each training case was determined by subtracting the steady-state temperature for the 0 mm reduction case from the steady-state temperature for the case in question (for example, for the case of a water temperature of 80°C and a reduction of 2.25 mm, the steady state temperature for 80°C water temperature and 0 mm reduction was subtracted from the steady-state temperature for 2.25 mm reduction to determine the damage metric value).

Simulations to produce data for ten test cases were also performed. Wall thickness, water temperature, thermal conductivity, density, specific heat, internal convection coefficient, external heat transfer coefficient, and surrounding air temperature were all assigned uniform distributions varying between $\pm$10% of their expected values, and values for each parameter were randomly selected for the ten cases. Two simulations were performed to produce the test data for each of the ten cases. The first simulation used the varied parameter values but used no thickness reduction, while the second simulation utilized the varied thickness reduction value as well. The change in the steady-state temperature between the "current" thickness reduction and the initial thickness reduction could then be computed by determining the difference in steady-state temperatures between the second and first simulations. Gaussian white noise (GWN) was added to the testing data. To ensure that the standard deviation value used for the GWN was a realistic amount, a suitable value was determined by collecting room temperature data with several calibrated T-type thermocouples and determining the mean standard deviation of the measured temperatures for all tested thermocouples. The standard deviation value determined from this test was 0.1°C, so that value was used for the GWN added to the testing data. The parameter values used for the ten test cases are shown in Table 4.2. A plot of the temperature time histories at steady state (including noise) for all cases, and a plot showing the change in mean steady-state temperature between the initial state and the current state for all cases are shown in Figure 4.3. The results shown in Figure 4.3 highlight how different the steady-state temperatures are for each case.

Table 4. 2: Parameter values for each of the ten test cases

Parameter	Thickness reduction (mm)	*k (W/mK)*	ρ (kg/m^3)	C_p (J/kgK)	h_i (W/m^{2}K)	h_{ins} (W/m^{2}K)	T_w (°C)	T_{surr} (°C)
Case 1	1.66	14.2	7638	584	60.2	12.7	72.5	24.8
Case 2	0.80	15.2	8056	617	63.8	14.0	77.5	21.2
Case 3	2.14	15.6	7176	627	57.3	13.6	81.1	25.1
Case 4	3.20	14.6	7924	595	56.4	12.1	84.5	21.8
Case 5	1.03	16.0	7248	607	53.4	12.5	82.2	22.5
Case 6	2.90	15.6	7442	551	62.8	12.0	86.4	20.8
Case 7	0.37	14.0	8425	660	58.1	11.6	79.7	22.7
Case 8	2.60	16.5	7803	561	59.3	12.8	76.4	23.4
Case 9	4.47	13.6	8250	572	62.4	13.2	74.6	23.7
Case 10	3.67	14.7	8569	640	54.7	13.7	86.3	24.2

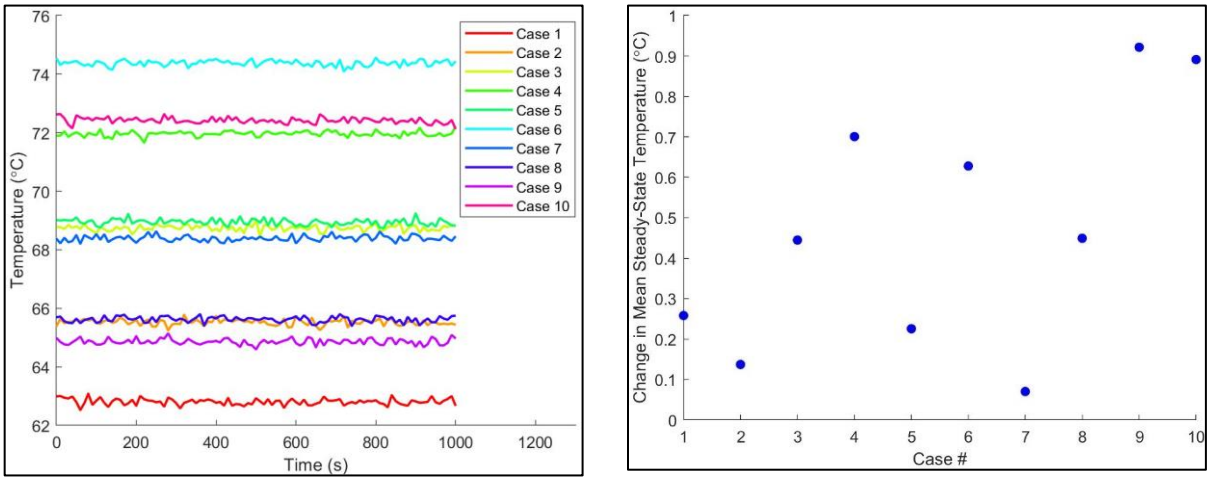

(a) (b)

Figure 4. 3: Plots showing the temperature time histories at steady-state for each case (a) and the change in steady-state temperature from the zero-reduction state for each case (b)

In practice, the effect of measurement noise can be reduced by averaging the measured temperatures over a long period of time. Therefore, the steady-state temperatures for the testing data were determined by averaging the noisy simulation data over a period of 1000 seconds (100 samples). These mean steady-state temperatures were then used as inputs into both GPM1 and GPM2 to estimate the thickness reduction value. GPM2 was also fed the correct water temperature as an input. The results of the estimations are shown below in Figure 4.4.

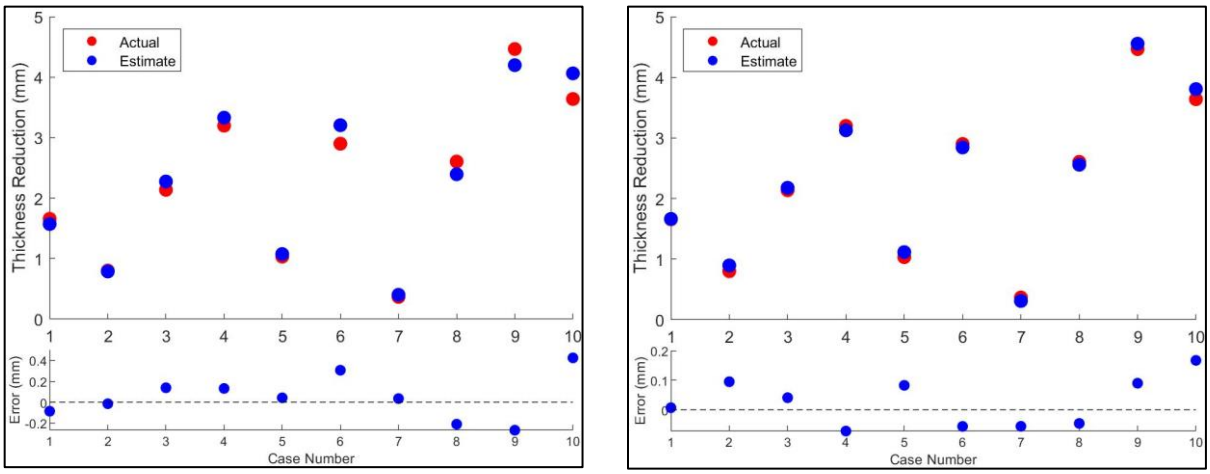

(a) (b)

Figure 4. 4: Thickness reduction estimates of GPM1 (a) and GPM2 (b) compared to actual thickness reductions

As shown in Figure 4.4(a), GPM1 is able to produce accurate results, despite the inclusion of measurement noise and up to 10% variations in the model parameters compared to the expected parameter values used for training of the model. Errors remain below 0.5 mm for all cases, meaning that the errors remain below 9% of the original pipe thickness.

If the mean water temperature is known during the measurement periods for both the initial, non-reduction case and the current measurement, the accuracy of the technique can be improved, in general. As shown in Figure 4.4(b), when using both the water temperature and the change in steady-state temperature from the non-reduction state as inputs to GPM2, the errors between the estimated thickness reductions and the actual thickness reductions reduce

for most cases. Despite the fact that the errors for some cases increase slightly, the maximum error produced for any of the cases decreased. Errors remained below 0.2 mm for all cases, or 3.6% of the original pipe thickness.

4.3 Conclusions

In this chapter, a technique for estimating the reduction in wall thickness of an insulated carbon steel pipe elbow in a nuclear power plant piping system was described. A heat conduction model for the heat transfer between the water in the pipe and the pipe itself was implemented. An approximation of the heat transfer physics of the insulation was performed in order to reduce computation time for the training and testing simulations required for both implementation and verification of the estimation technique. A sensitivity analysis was also performed to establish which model parameters had the greatest effect on the steady-state. Water temperature was found to dominate the other parameters in terms of the impact of its variance on the variance of the steady-state temperature. Because of this, two surrogate (GPR) models to estimate wall thickness reduction were studied, one using just the change in measured steady-state temperature from the initial measurement with no thickness reduction and the "current" measurement as an input, and one using water temperature as an additional input. Both GPR models were shown to be fairly accurate, despite variations in the model parameters from those that were used to train the GPR models. GPM2 was shown to me more accurate in general, though this model also required one more input that GPM1. The study of this technique provides a promising outlook for the possibility of applying the technique to detect wall thinning in pipe elbows. The ease of use and cost-effectiveness of the technique are primary advantages that the method has over current pipe inspection methods.

Chapter 5. Conclusions and Future Work

5.1 Conclusions

In this dissertation, two passive NDE methods that utilize temperature measurements were developed and analyzed. For the first method, described in Chapter 2, a flaw identification technique for curing FRP composites, a KF-based temperature estimation technique that utilized IR thermography surface temperature measurements to perform estimations in real-time was first developed. Despite various simplifying approximations made in the model, the method's ability to accurately estimate internal temperatures was validated using experimental data collected from a section of a wind turbine blade during cure. The error in mean estimated temperatures as compared to measured internal temperatures was less than 5% for all times not including the initial infusion period and the temperature rise. The estimated mean temperature at during the temperature rise experienced 5-15% errors at all internal measurement locations. The method was demonstrated to have the ability to perform real-time estimations. To the best of authors' knowledge, this is the only study to date to discuss real-time monitoring for resin systems with complex free-radical polymerization reactions experiencing autoacceleration.

In Chapter 3, a technique for detecting flaws in FRP composites during the curing process using IR thermography measurements, the temperature estimation method described in Chapter 2, and the CCT (a metric computed from the Kalman filter corrections) was described. The ability of the temperature estimation technique to improve temperature estimation accuracy in the presence of flaws was verified using simulation-based data. The flaw detection method's effectiveness was also evaluated using simulation-based verification case studies. The method showed the ability to identify resin-rich areas of an FRP composite well, but identification of resin-deficient regions internal to the part required the use of a less-strict outlier criterion. Similar performance was observed when using an incorrectly-assumed model as the base heat conduction model. One false positive was produced, but this issue can likely be solved with the use of noise-reduction measures. The technique's ability to identify multiple flaws was also evaluated. When both a near-surface and deep flaw were present, the technique only identified the near-surface flaw, unless the deeper flaw resulted in significant deviation from the expected behavior than the near-surface flaw. This would not be an inhibition to implementing this technique in an industrial setting, however, as the identification of one flaw would indicate that the part should be thoroughly evaluated in post-manufacturing inspection.

In Chapter 4, a technique for estimating the reduction in wall thickness of an insulated carbon steel pipe elbow in a nuclear power plant piping system was described. A sensitivity analysis was performed to establish which model parameters had the greatest effect on the steady-state temperatures. Water temperature was found to dominate the other parameters in terms of the impact of its variance on the variance of the steady-state temperature. Because of this, two surrogate (GPR) models to estimate wall thickness reduction were studied, one using just the change in measured steady-state temperature from the initial measurement with no thickness reduction and the current measurement as an input, and one using water temperature as an additional input. Both GPR models were shown to be fairly accurate, despite variations in the model parameters from those that were used to train the GPR models. The GPR model with water temperature as an additional input was shown to me more accurate in general. The ease of use and cost-effectiveness of the technique are primary advantages that the method has over current pipe inspection methods for identifying FAC-induced wall thinning.

5.2 Future Work

In the future, the temperature estimation technique described in Chapter 2 can potentially be used to aid in identifying flaws such as poor resin distribution or residual stresses during the curing process, which can save time and resources by reducing the amount of post-manufacturing inspection required for the part. As noted in Chapter 1, residual stress estimation requires the use of both temperature and degree of cure fields, both of which are estimated using the technique described in Chapter 2. The aforementioned flaw identification, along with degree of cure estimation, can help reduce the time and resources spent on FRP composite manufacturing, which will in turn aid in bringing FRP composites into lower-cost, higher volume manufacturing applications.

Future work for the flaw detection method for curing FRP composite, described in Chapter 3, can include the verification of the technique in other situations when the assumed model does not match the true physics of the curing composite. An incorrectly-assumed cure kinetics model was studied in this work, but cases such as those when the properties of the composite part (or the evolution of those properties, omitted from this study) are incorrectly assumed can also be evaluated. An investigation into methods to improve the detection capabilities of the technique in resin-deficient regions would be greatly beneficial. The improvement of the computational efficiency of the technique is also a necessity in order to enable real-time flaw detection in curing composites. The potential for the use of an

ensemble of KF-based estimators, each performed for one measurement point and a one-dimensional domain through the thickness can be evaluated for this purpose. Performing many 1D KF-based estimations, as opposed to one 3D estimation, is computationally-efficient due to the removal of the most computationally-demanding step of the KF computation, the inversion of $\boldsymbol{S}$ (which becomes a scalar when there is only one measurement point). As such, an optimization of the number of measurement points required in order to maintain accuracy can also be performed to potentially aid in reducing the computation time. In order to utilize the ensemble of KF-based estimators approach, the improvement in computational speed would need to be weighed against any reductions in accuracy as a result of omitting the effects of internal heat conduction in the XY plane. Some information about the heat conduction in the XY plane would be captured in the variations in the measurements across the top surface, but it is unclear whether this information would be enough to identify flaws in the XY plane or not.

The potential utility of the technique explored for identifying FAC-induced wall thinning in pipes in Chapter 4 as a passive, first-warn method for identifying wall thinning, or possibly as a standalone technique, requires further research to be fully evaluated. The ability to estimate the water temperature using additional mounted thermocouples on the pipe would allow water temperature to be used as an input to the GPR model (assuming the mean water temperature was not already being measured), which was shown to improve accuracy. Future work studying the effectiveness of a steady-state temperature-based technique for other pipe features that are susceptible to FAC-induced rupture, such as T-joints or sections immediately following valves or reducers can be performed. The technique described above is well-equipped to identify wall thinning in pipe sections that experience non-symmetrical FAC, such as elbows or T-joints. Further research is required to determine its effectiveness for pipe sections that experience symmetrical FAC. Additionally, the effect of the oxide layer that builds up on the inside surface of the pipe on the heat transfer properties was not considered in this study. The oxide layer has been shown to provide a thermal resistance, so inclusion of these effects in the simulation model used to train GPR model would both enable a more thorough study of the utility of the technique and would potentially enable the technique to be effectively demonstrated for field use. Experimental validation of the technique would also be a useful endeavor for evaluating the method's suitability for real application.

References

[1] Chen X, Zhao W, Zhao XL, Xu JZ. Preliminary failure investigation of a 52.3m glass/epoxy composite wind turbine blade. Eng Fail Anal 2014;44:345–50. doi:10.1016/j.engfailanal.2014.05.024.

[2] Wu PC. Erosion/Corrosion-induced Pipe Wall Thinning in U.S. Nuclear Power Plants. U.S. Department of Energy: 1989. doi:10.2172/6152848.

[3] Ahmed WH. Evaluation of the proximity effect on flow-accelerated corrosion. Ann Nucl Energy 2010;37:598–605. doi:10.1016/j.anucene.2009.12.020.

[4] Ibrahim ME. Nondestructive evaluation of thick-section composites and sandwich structures: A review. Compos Part A Appl Sci Manuf 2014;64:36–48. doi:10.1016/j.compositesa.2014.04.010.

[5] Maierhofer C, Myrach P, Reischel M, Steinfurth H, Röllig M, Kunert M. Characterizing damage in CFRP structures using flash thermography in reflection and transmission configurations. Compos Part B Eng 2014;57:35–46. doi:10.1016/j.compositesb.2013.09.036.

[6] Wu D, Busse G. Lock-in thermography for nondestructive evaluation of materials. Rev Gen Therm 1998;37:693–703. doi:10.1016/S0035-3159(98)80047-0.

[7] Manohar A, Lanza di Scalea F. Detection of defects in wind turbine composite blades using statistically enhanced Lock-In Thermography. Struct Heal Monit 2013;12:566–74. doi:10.1177/1475921713498531.

[8] Ryu CH, Park SH, Kim DH, Jhang KY, Kim HS. Nondestructive evaluation of hidden multi-delamination in a glass-fiber-reinforced plastic composite using terahertz spectroscopy. Compos Struct 2016;156:338–47. doi:10.1016/j.compstruct.2015.09.055.

[9] Raiˇsutis R, Jasiunien_e E, ˇSliteris R VA. The review of non-destructive testing techniques suitable for inspect manufacturing of the wind turbine blades. 2008;63:63(1):26–30.

[10] Al-Naemi FI, Hall JP, Moses AJ. FEM modelling techniques of magnetic flux leakage-type NDT for ferromagnetic plate inspections. J Magn Magn Mater 2006;304:e790–3. doi:10.1016/j.jmmm.2006.02.225.

[11] Singh WS, Rao BPC, Vaidyanathan S, Jayakumar T, Raj B. Detection of leakage magnetic flux from near-side and far-side defects in carbon steel plates using a giant magneto-resistive sensor. Meas Sci Technol 2008;19:015702. doi:10.1088/0957-0233/19/1/015702.

[12] Hollaway LC. A review of the present and future utilisation of FRP composites in the civil infrastructure with reference to their important in-service properties. Constr Build Mater 2010;24:2419–45. doi:10.1016/J.CONBUILDMAT.2010.04.062.

[13] Lubin G. Handbook of Composites. Springer Science & Business Media; 2013.

[14] Mangalgiri PD. Composite materials for aerospace applications. Bull Mater Sci 1999;22:657–64. doi:10.1007/BF02749982.

[15] Friedrich K, Almajid AA. Manufacturing Aspects of Advanced Polymer Composites for Automotive Applications. Appl Compos Mater 2013;20:107–28. doi:10.1007/s10443-012-9258-7.

[16] Vaidya U. Advanced Composite Materials and Manufacturing in Vehicles, Wind, and Compressed Gas Storage. Text World 2017.

[17] DOE, Office AM. Fiber Reinforced Polymer Composite Manufacturing RFI: Summary of Responses. 2013.

[18] Konstantopoulos S, Fauster E, Schledjewski R. Monitoring the production of FRP composites: A review of in-line sensing methods. Express Polym Lett 2014;8:823–40. doi:10.3144/expresspolymlett.2014.84.

[19] Schubel PJ, Crossley RJ, Boateng EKG, Hutchinson JR. Review of structural health and cure monitoring techniques for large wind turbine blades. Renew Energy 2013;51:113–23. doi:10.1016/J.RENENE.2012.08.072.

[20] Parthasarathy S, Mantell SC, Stelson KA. Estimation, control and optimization of curing in thick-sectioned composite parts. J Dyn Syst Meas Control Trans ASME 2004;126:824–33. doi:10.1115/1.1850536.

[21] Lee JH, Lee SJ. Application of laser-generated guided wave for evaluation of corrosion in carbon steel pipe. NDT E Int 2009;42:222–7. doi:10.1016/j.ndteint.2008.09.011.

[22] Nasrazadani S, Nakka RK, Hopkins D, Stevens J. Characterization of oxides on FAC susceptible small-bore

carbon steel piping of a power plant. Int J Press Vessel Pip 2009;86:845–52. doi:10.1016/j.ijpvp.2009.10.003.

[23] Leng JS, Asundi A. Real-time cure monitoring of smart composite materials using extrinsic Fabry-Perot interferometer and fiber Bragg grating sensors. Smart Mater Struct 2002;11:249–55. doi:10.1088/0964-1726/11/2/308.

[24] Murukeshan VM, Chan PY, Ong LS, Seah LK. Cure monitoring of smart composites using Fiber Bragg Grating based embedded sensors. Sensors Actuators A Phys 2000;79:153–61. doi:10.1016/S0924-4247(99)00266-6.

[25] Kang HK, Kang DH, Bang HJ, Hong CS, Kim CG. Cure monitoring of composite laminates using fiber optic sensors. Smart Mater Struct 2002;11:279–87. doi:10.1088/0964-1726/11/2/311.

[26] Jang BZ, Shih WK. Techniques for cure monitoring of thermoset resins and composites - a review. Mater Manuf Process 1990;5:301–31. doi:10.1080/10426919008953248.

[27] Antonucci V, Giordano M, Cusano A, Nasser J, Nicolais L. Real time monitoring of cure and gelification of a thermoset matrix. Compos Sci Technol 2006;66:3273–80. doi:10.1016/J.COMPSCITECH.2005.07.009.

[28] Tuncol G, Danisman M, Kaynar A, Sozer EM. Constraints on monitoring resin flow in the resin transfer molding (RTM) process by using thermocouple sensors. Compos Part A Appl Sci Manuf 2007;38:1363–86. doi:10.1016/J.COMPOSITESA.2006.10.009.

[29] Hsiao K-T, Little R, Restrepo O, Minaie B. A study of direct cure kinetics characterization during liquid composite molding. Compos Part A Appl Sci Manuf 2006;37:925–33. doi:10.1016/J.COMPOSITESA.2005.01.019.

[30] Lionetto F, Maffezzoli A. Monitoring the cure state of thermosetting resins by ultrasound. Materials (Basel) 2013;6:3783–804. doi:10.3390/ma6093783.

[31] Lionetto F, Tarzia A, Maffezzoli A. Air-coupled ultrasound: A novel technique for monitoring the curing of thermosetting matrices. IEEE Trans Ultrason Ferroelectr Freq Control 2007;54:1437–43. doi:10.1109/TUFFC.2007.404.

[32] Konstantopoulos S, Tonejc M, Maier A, Schledjewski R. Exploiting temperature measurements for cure

monitoring of FRP composites—Applications with thermocouples and infrared thermography. J Reinf Plast Compos 2015;34:1015–26. doi:10.1177/0731684415586611.

[33] Milošević ND, Raynaud M. Analytical solution of transient heat conduction in a two-layer anisotropic cylindrical slab excited superficially by a short laser pulse. Int J Heat Mass Transf 2004;47:1627–41. doi:10.1016/j.ijheatmasstransfer.2003.10.023.

[34] Ji CC, Tuan PC, Jang HY. A recursive least-squares algorithm for on-line 1-D inverse heat conduction estimation. Int J Heat Mass Transf 1997;40:2081–96. doi:10.1016/S0017-9310(96)00289-X.

[35] Raynaud M, Beck J V. Methodology for comparison of inverse heat conduction methods. J Heat Transfer 1988;110:30–7. doi:10.1115/1.3250468.

[36] D'Antona G, Seifnaraghi N. Temperature Distribution Reconstruction by Eigenfunction Interpolation of Boundary Measurement Data. IEEE Trans Instrum Meas 2014;63:334–42. doi:10.1109/TIM.2013.2280476.

[37] Shang-bin J, Xiao-xue Q, Ding L, Yang L, Yuan C. Research on method of reconstructing temperature field of silicon melt based on eigenfunction interpolation. 2018 13th IEEE Conf. Ind. Electron. Appl., IEEE; 2018, p. 329–34. doi:10.1109/ICIEA.2018.8397737.

[38] Kalman RE. A New Approach to Linear Filtering and Prediction Problems. Trans ASME-Journal Basic Eng 1960:35–45.

[39] Wan EA, Van Der Merwe R. The unscented Kalman filter for nonlinear estimation. IEEE 2000 Adapt. Syst. Signal Process. Commun. Control Symp. AS-SPCC 2000, IEEE; 2000, p. 153–8. doi:10.1109/ASSPCC.2000.882463.

[40] Matsuzaki R, Tachikawa T, Ishizuka J. Estimation of state and material properties during heat-curing molding of composite materials using data assimilation: A numerical study. Heliyon 2018;4:e00554. doi:10.1016/j.heliyon.2018.e00554.

[41] Dai H, Zhu L, Zhu J, Wei X, Sun Z. Adaptive Kalman filtering based internal temperature estimation with an equivalent electrical network thermal model for hard-cased batteries. J Power Sources 2015;293:351–65. doi:10.1016/J.JPOWSOUR.2015.05.087.

[42] Youngki Kim, Mohan S, Siegel JB, Stefanopoulou AG, Yi Ding. The Estimation of Temperature Distribution in Cylindrical Battery Cells Under Unknown Cooling Conditions. IEEE Trans Control Syst Technol 2014;22:2277–86. doi:10.1109/TCST.2014.2309492.

[43] Skordos AA, Partridge IK. Inverse heat transfer for optimization and on-line thermal properties estimation in composites curing. Inverse Probl Sci Eng 2004;12:157–72. doi:10.1080/10682760310001598616.

[44] Scott EP, Beck J V. Estimation of Thermal Properties in Carbon/Epoxy Composite Materials during Curing. J Compos Mater 1992;26:20–36. doi:10.1177/002199839202600102.

[45] Wieland B, Ropte S, Wieland B, Ropte S. Process Modeling of Composite Materials for Wind-Turbine Rotor Blades: Experiments and Numerical Modeling. Materials (Basel) 2017;10:1157. doi:10.3390/ma10101157.

[46] Twardowski TE, Lin SE, Geil PH. Curing in Thick Composite Laminates: Experiment and Simulation. J Compos Mater 1993;27:216–50. doi:10.1177/002199839302700301.

[47] Dorgan J, Wassgren J, Cousins D, Suzuki Y, Kappes BB, Stebner AP. Kinetics and temperature evolution during the bulk polymerization of methyl methacrylate for vacuum-assisted resin transfer molding. Compos Part A Appl Sci Manuf 2017;104:60–7. doi:10.1016/j.compositesa.2017.10.022.

[48] Bakhtiary Davijani AA, Hajikhani M, Ahmadi M. Acoustic Emission based on sentry function to monitor the initiation of delamination in composite materials. Mater Des 2011;32:3059–65. doi:10.1016/j.matdes.2011.01.010.

[49] Prakash R. NON-DESTRUCTIVE TESTING OF COMPOSITES. Composites 1980;11:217–24. doi:10.1016/0010-4361(80)90428-0.

[50] Ray BC, Hasan ST, Clegg DW. Evaluation of Defects in FRP Composites by NDT Techniques. J Reinf Plast Compos 2007;26:1187–92. doi:10.1177/0731684407079348.

[51] Parlevliet PP, Bersee HEN, Beukers A. Residual stresses in thermoplastic composites—A study of the literature—Part I: Formation of residual stresses. Compos Part A Appl Sci Manuf 2006;37:1847–57. doi:10.1016/J.COMPOSITESA.2005.12.025.

[52] Parlevliet PP, Bersee HEN, Beukers A. Residual stresses in thermoplastic composites – a study of the

literature. Part III: Effects of thermal residual stresses. Compos Part A Appl Sci Manuf 2007;38:1581–96. doi:10.1016/J.COMPOSITESA.2006.12.005.

[53] Bagavathiappan S, Lahiri BB, Saravanan T, Philip J, Jayakumar T. Infrared thermography for condition monitoring - A review. Infrared Phys Technol 2013;60:35–55. doi:10.1016/j.infrared.2013.03.006.

[54] Manohar A, Lanza di Scalea F. Determination of Defect Depth and Size Using Virtual Heat Sources in Pulsed Infrared Thermography. Exp Mech 2013;53:661–71. doi:10.1007/s11340-012-9670-9.

[55] Cuevas E, García C, Hernandez S, Gomez T, Cañada M. Non destructive testing for non cured composites: Air coupled Ultrasounds and Thermography. 5th Int. Symp. NDT Aerosp., 2013, p. 13–5.

[56] Nassr AA, El-Dakhakhni WW. Non-destructive evaluation of laminated composite plates using dielectrometry sensors. Smart Mater Struct 2009;18:055014. doi:10.1088/0964-1726/18/5/055014.

[57] Chang F, Couchman J, Eisenmann J, Yee B. Application of a Special X-Ray Nondestructive Testing Technique for Monitoring Damage Zone Growth in Composite Laminates. Compos. Reliab., ASTM International; 2009, p. 176-176–15. doi:10.1520/stp32307s.

[58] Jördens C, Wietzke S, Scheller M, Koch M. Investigation of the water absorption in polyamide and wood plastic composite by terahertz time-domain spectroscopy. Polym Test 2010;29:209–15. doi:10.1016/j.polymertesting.2009.11.003.

[59] Park JW, Im KH, Hsu DK, Jung JA, Yang IY. Terahertz spectroscopy approach of the fiber orientation influence on CFRP composite solid laminates. J Mech Sci Technol 2012;26:2051–4. doi:10.1007/s12206-012-0513-5.

[60] Kain V, Roychowdhury S, Mathew T, Bhandakkar A. Flow accelerated corrosion and its control measures for the secondary circuit pipelines in Indian nuclear power plants. J Nucl Mater 2008;383:86–91. doi:10.1016/j.jnucmat.2008.08.024.

[61] Somerscales EFC. Fundamentals of corrosion fouling. Exp Therm Fluid Sci 1997;14:335–55. doi:10.1016/S0894-1777(96)00136-7.

[62] Somerscales EFC, Sanatgar H. Hydrodynamic removal of corrosion products from a surface. Br Corros J

1992;27:36–44. doi:10.1179/000705992798268846.

[63] Kain V, Roychowdhury S, Ahmedabadi P, Barua DK. Flow accelerated corrosion: Experience from examination of components from nuclear power plants. Eng Fail Anal 2011;18:2028–41. doi:10.1016/j.engfailanal.2011.06.007.

[64] Yi W-G, Lee M-R, Lee J-H, Lee S-H. A STUDY ON THE ULTRASONIC THICKNESS MEASUREMENT OF WALL THINNED PIPE IN NUCLEAR POWER PLANTS. n.d.

[65] Ting K, Ma YP. Evaluation of erosion/corrosion problems of carbon steel piping in Taiwan PWR nuclear power plant. Nucl Eng Des 1999;191:231–43. doi:10.1016/S0029-5493(99)00145-4.

[66] Huthwaite P, Ribichini R, Cawley P, Lowe M. Mode selection for corrosion detection in pipes and vessels via guided wave tomography. IEEE Trans Ultrason Ferroelectr Freq Control 2013;60:1165–77. doi:10.1109/TUFFC.2013.2679.

[67] Vanaei HR, Eslami A, Egbewande A. A review on pipeline corrosion, in-line inspection (ILI), and corrosion growth rate models. Int J Press Vessel Pip 2017;149:43–54. doi:10.1016/j.ijpvp.2016.11.007.

[68] Angani CS, Park DG, Kim GD, Kim CG, Cheong YM. Differential pulsed eddy current sensor for the detection of wall thinning in an insulated stainless steel pipe. J Appl Phys 2010;107:2. doi:10.1063/1.3337725.

[69] Cheng W. Pulsed eddy current testing of carbon steel pipes' wall-thinning through insulation and cladding. J Nondestruct Eval 2012;31:215–24. doi:10.1007/s10921-012-0137-9.

[70] Safizadeh MS, Azizzadeh T. Corrosion detection of internal pipeline using NDT optical inspection system. NDT E Int 2012;52:144–8. doi:10.1016/j.ndteint.2012.07.008.

[71] Kamachi Mudali U, Babu Rao C, Raj B. Intergranular corrosion damage evaluation through laser scattering technique. Corros Sci 2006;48:783–96. doi:10.1016/j.corsci.2005.02.027.

[72] Mazumdar A, Lozano M, Fittery A, Asada HH. A compact, maneuverable, underwater robot for direct inspection of nuclear power piping systems. Proc. - IEEE Int. Conf. Robot. Autom., Institute of Electrical and Electronics Engineers Inc.; 2012, p. 2818–23. doi:10.1109/ICRA.2012.6224619.

[73] Mackenzie LD, Pierce SG, Hayward G. Robotic inspection system for non-destructive evaluation (NDE) of pipes. AIP Conf. Proc., vol. 1096, American Institute of Physics; 2009, p. 1687–94. doi:10.1063/1.3114161.

[74] Choi C, Park B, Jung S. The design and analysis of a feeder pipe inspection robot with an automatic pipe tracking system. IEEE/ASME Trans Mechatronics 2010;15:736–45. doi:10.1109/TMECH.2009.2032541.

[75] Gustafson K, Abe T. The third boundary condition—was it robin's? Math Intell 1998;20:63–71. doi:10.1007/BF03024402.

[76] Incropera FP, DeWitt DP, Bergman TL, Lavine AS. Fundamentals of Heat and Mass Transfer-Incropera. Wiley; 2007.

[77] Tang X, Zhao X, Zhang X. The square-root spherical simplex unscented Kalman filter for state and parameter estimation. Int. Conf. Signal Process. Proceedings, ICSP, vol. 6, IEEE; 2008, p. 260–3. doi:10.1109/ICOSP.2008.4697120.

[78] COMSOL Inc. COMSOL Multiphysics Reference Manual, version 5.3 n.d.

[79] Trommsdorff VE, Köhle H, Lagally P. Zur polymerisation des methacrylsäuremethylesters1. Die Makromol Chemie 1948;1:169–98. doi:10.1002/macp.1948.020010301.

[80] Sobol IM. Global sensitivity indices for nonlinear mathematical models and their Monte Carlo estimates. Math Comput Simul 2001;55:271–80. doi:10.1016/S0378-4754(00)00270-6.

[81] Saltelli A, Annoni P, Azzini I, Campolongo F, Ratto M, Tarantola S. Variance based sensitivity analysis of model output. Design and estimator for the total sensitivity index. Comput Phys Commun 2010;181:259–70. doi:10.1016/j.cpc.2009.09.018.

[82] Smith M. ABAQUS/Standard User's Manual, Version 6.9 2009.

Appendices

Appendix A: Details of the Finite Difference Scheme for Heat Conduction

The finite-difference nodal network used for the approximation of the heat equation was set up so that node 1 was at the top-left corner of the domain, and final node was at the bottom right corner of the domain. A diagram describing the nodal layout is shown below in Figure A.1. The number of nodes in the *x*-direction is *M* and the number of nodes in the *y*-direction is *N*.

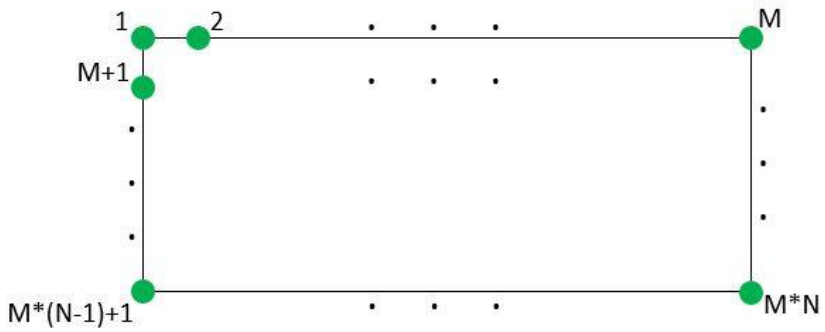

Figure A. 1: Diagram showing the numbered nodal layout

A five-point stencil can be used to describe the relative position of nodes for a 2D centered-in-space FD approximation.

Solving for the value of the states at the central node requires values from the four surrounding nodes. The five-point Stencil is shown in Figure A.2.

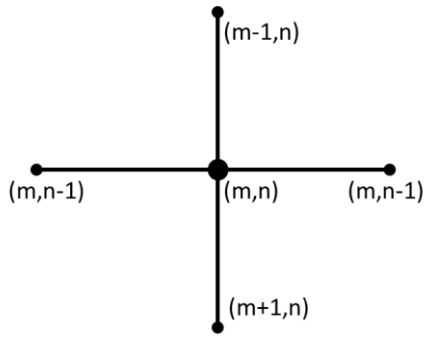

Figure A. 2: Five-point Stencil for a 2D centered-in-space FD network

In Chapter 2, the form of the FTCS approximation of the heat equation was shown. Below is a derivation showing the specifics of the diffusivity matrix, $\boldsymbol{M}$, for non-boundary nodes. Assuming an isotropic, homogeneous medium and no heat transfer in the *z* direction, the heat equation can be represented as:

$$\frac{\partial \boldsymbol{\theta}}{\partial t} = \frac{k}{\rho C_p}\left(\frac{\partial^2 \boldsymbol{\theta}}{\partial x^2} + \frac{\partial^2 \boldsymbol{\theta}}{\partial y^2}\right) + \frac{1}{\rho C_p} f(\boldsymbol{\theta}, \boldsymbol{\varphi}). \qquad (A.1.1)$$

Equation A.1.1 can be approximated using FTCS for 2D at time step *i*, column *m*, and row *n* as:

$$\frac{\theta_{m,n}^{i} - \theta_{m,n}^{i-1}}{\Delta t} = \frac{k}{\rho C_p}\frac{\theta_{m-1,n}^{i-1} - 2\theta_{m,n}^{i-1} + \theta_{m+1,n}^{i-1}}{\Delta x^2} + \frac{k}{\rho C_p}\frac{\theta_{m,n-1}^{i-1} - 2\theta_{m,n}^{i-1} + \theta_{m,n+1}^{i-1}}{\Delta y^2} + \frac{1}{\rho C_p} f_{m,n}^{i-1}, \qquad (A.1.2)$$

where the spatial steps in the x and y direction for the finite difference network were defined as Δx and Δy, respectively. Let

$$r_x = \frac{k\Delta t}{\rho C_p \Delta x^2};\ r_y = \frac{k\Delta t}{\rho C_p \Delta y^2}.$$

Therefore, Equation A.1.2 above can be simplified as:

$$\theta_{m,n}^{i} = \left(1 - 2r_x - 2r_y\right)\theta_{m,n}^{i-1} + r_x\left(\theta_{m-1,n}^{i-1} + \theta_{m+1,n}^{i-1}\right) + r_y\left(\theta_{m,n-1}^{i-1} + \theta_{m,n+1}^{i-1}\right) + \frac{\Delta t}{\rho C_p} f_{m,n}^{i-1}, \qquad (A.1.3)$$

which can be represented in matrix form as:

$$\boldsymbol{\theta}^{i} = \boldsymbol{M}\boldsymbol{\theta}^{i-1} + \frac{\Delta t}{\rho C_p}\boldsymbol{f}^{i-1}, \qquad (A.1.4)$$

where $\boldsymbol{f}^{i-1}$ is computed as described in Chapter 2. For non-boundary nodes, the $\boldsymbol{M}$ matrix is:

$$\boldsymbol{M} = \begin{bmatrix} \ddots & \ddots & \ddots & \ddots & \ddots & \ddots & \ddots & \ddots & \ddots & \ddots & \ddots & \ddots & \ddots & \ddots & & \\ \ddots & 0 & r_y & 0 & \cdots & 0 & r_x & 1-2r_x-2r_y & r_x & 0 & \cdots & 0 & r_y & 0 & \ddots & \\ & \ddots & 0 & r_y & 0 & \cdots & 0 & r_x & 1-2r_x-2r_y & r_x & 0 & \cdots & 0 & r_y & 0 & \ddots \\ & & \ddots & 0 & r_y & 0 & \cdots & 0 & r_x & 1-2r_x-2r_y & r_x & 0 & \cdots & 0 & r_y & 0 \\ & & & \ddots & \ddots & \ddots & \ddots & \ddots & \ddots & \ddots & \ddots & \ddots & \ddots & \ddots & \ddots & \ddots \end{bmatrix}.$$

For boundary nodes, an equation for ghost nodes must be derived in order to substitute into Equation A.1.4 above. The equation for the rate of heat flow at the boundaries is:

$$\boldsymbol{n} \cdot k\boldsymbol{\nabla\theta} = \boldsymbol{q}, \qquad (A.1.5)$$

where $\boldsymbol{q}$ is the heat transferred through the boundary, and $\boldsymbol{n}$ is the unit normal vector for the surface. The boundaries are labeled in Figure 2.1, but for convenience, the top boundary is Γ_T, the left boundary is Γ_L, the right boundary is Γ_T, and the bottom boundary is Γ_B. The boundaries at Γ_T and Γ_B will be used as examples. For the boundary at Γ_T, Equation A.1.5 can be approximated using a central difference equation as follows:

$$-k\frac{\theta^i_{m,0} - \theta^i_{m,2}}{2\Delta y} = h\left(\theta^i_{m,1} - \theta_{surr}\right), \qquad (A.1.6)$$

which simplifies to the following expression for the top ghost nodes:

$$\theta^i_{m,0} = \frac{-2h\Delta y}{k}\theta^i_{m,1} + \theta^i_{m,2} + \frac{2h\Delta y}{k}\theta_{surr}. \qquad (A.1.7)$$

For the boundary at Γ_B, Equation A.1.5 can be approximated using a central difference equation as follows:

$$k\frac{\theta^i_{m,n+1} - \theta^i_{m,n-1}}{2\Delta y} = -h_{bot}\left(\theta^i_{m,n} - \theta_{mold}\right), \qquad (A.1.8)$$

which simplifies to the following expression for the bottom ghost nodes:

$$\theta^i_{m,n+1} = \frac{-2h_{bot}\Delta y}{k}\theta^i_{m,n} + \theta^i_{m,n-1} + \frac{2h_{bot}\Delta y}{k}\theta_{mold}. \qquad (A.1.9)$$

These expressions were substituted into Equation A.1.4 at the boundary nodes. For example, substituting Equation A.1.7 into Equation A.1.4 yields:

$$\theta^i_{m,1} = \left(1-2r_x-2r_y\right)\theta^{i-1}_{m,1} + r_x\left(\theta^{i-1}_{m-1,1} + \theta^{i-1}_{m+1,1}\right) + r_y\left(\frac{-2h\Delta y}{k}\theta^{i-1}_{m,1} + \theta^{i-1}_{m,2} + \frac{2h\Delta y}{k}\theta_{surr} + \theta^{i-1}_{m,2}\right) + \frac{\Delta t}{\rho C_p}f^{i-1}_{m,1}, \quad (A.1.10)$$

which simplifies to:

$$\theta^i_{m,1} = \left(1-2r_x-2r_y-\frac{2hr_y\Delta y}{k}\right)\theta^{i-1}_{m,1} + r_x\left(\theta^{i-1}_{m-1,1} + \theta^{i-1}_{m+1,1}\right) + 2r_y\theta^{i-1}_{m,2} + \frac{2hr_y\Delta y}{k}\theta_{surr} + \frac{\Delta t}{\rho C_p}f^{i-1}_{m,1}. \quad (A.1.11)$$

Therefore, the row of the $\boldsymbol{M}$ matrix row for this particular node (with an index of l) is:

$$M_{l,1:m*n} = \begin{bmatrix} \cdots & 0 & r_x & 1-2r_x-2r_y-\dfrac{2hr_y\Delta y}{k} & r_x & 0 & \cdots & 2r_y & 0 & \cdots \end{bmatrix},$$

while the term for the ***b*** vector for this particular node is:

$$b_l = \frac{2hr_y\Delta y}{k}\theta_{surr}.$$